




















Measuring the ISM Content of Nearby, Luminous, Type 1 and Type 2 QSOs through CO and [C II]

YUANZE LUO ¹, A. O. PETRIC ^{1,2}, R.M.J. JANSSEN ³, D. FADDA ², N. FLAGEY ², A. OMONT ⁴, A. M. JACOB ¹,
K. ROWLANDS ^{1,5}, K. ALATALO ^{1,2}, N. BILLOT ⁶, T. HECKMAN ^{1,7}, B. HUSEMANN ⁸, D. KAKKAD ², M. LACY ⁹,
J. MARSHALL,¹⁰ R. MINCHIN ¹¹, R. MINSLEY,¹² N. NESVADBA ¹³, J. A. OTTER ¹, P. PATIL ¹ AND T. URRUTIA ¹⁴

¹William H. Miller III Department of Physics and Astronomy, Johns Hopkins University, Baltimore, MD 21218, USA

²Space Telescope Science Institute, 3700 San Martin Dr, Baltimore, MD 21218, USA

³Jet Propulsion Laboratory, California Institute of Technology, Pasadena, CA 91109, USA

⁴Sorbonne Université, UPMC Université Paris 6 and CNRS, UMR 7095, Institut d'Astrophysique de Paris, France

⁵AURA for ESA, Space Telescope Science Institute, 3700 San Martin Drive, Baltimore, MD 21218, USA

⁶Université de Genève, Department of Astronomy, Chemin Pegasi 51/b, 1290 Versoix, Switzerland

⁷School of Earth and Space Exploration, Arizona State University, Tempe, AZ 85287-1404, USA

⁸European Organisation for the Exploitation of Meteorological Satellites, Eumetsat Allee 1, 64295 Darmstadt, Germany

⁹National Radio Astronomy Observatory, Charlottesville, VA 22903, USA

¹⁰Department of Astronomy and Astrophysics, University of California, Santa Cruz, CA 95064, USA

¹¹National Radio Astronomy Observatory, P.O. Box O, Socorro, NM 87801, USA

¹²Steward Observatory, University of Arizona, Tucson, AZ 85721, also Department of Planetary Sciences, USA

¹³Université Côte d'Azur, Observatoire de la Côte d'Azur, CNRS, Laboratoire Lagrange, Bd de l'Observatoire, CS 34229, 06304 Nice cedex 4, France

¹⁴Leibniz-Institut für Astrophysik, Potsdam (AIP), An der Sternwarte 16, 14482 Potsdam, Germany

ABSTRACT

We present observations of CO(1–0) and CO(2–1) lines from the Institut de radioastronomie millimétrique (IRAM) 30m telescope toward 20 nearby, optically luminous type 2 quasars (QSO2s) and observations of [C II] 158 μ m line from the Stratospheric Observatory For Infrared Astronomy (SOFIA) for 5 QSO2s in the CO sample and 5 type 1 quasars (QSO1s). In the traditional evolutionary scenario explaining different types of QSOs, obscured QSO2s emerge from gas-rich mergers observed as luminous infrared galaxies (LIRGs) and then turn into unobscured QSO1s as the black holes clear out the obscuring material in a blow-out phase. We test the validity of this theoretical prediction by comparing the gas fractions and star formation efficiencies among LIRGs and QSOs. We find that CO luminosity, CO-derived gas masses and gas fractions in QSO1s are consistent with those estimated for QSO2s, while LIRGs exhibit a closer resemblance to QSO2s in terms of CO-derived gas masses and gas fractions, and [C II] luminosity. However, comparisons between [C II] luminosity and star formation tracers such as the CO and infrared luminosity imply additional sources of [C II] emission in QSO1s likely tracing neutral atomic or ionized gas. All three types of galaxies have statistically indistinguishable distributions of star formation efficiency. Our results are consistent with part of the evolutionary scenario where nearby QSO2s could emerge from LIRGs, but they are unlikely to be the precursors of nearby QSO1s.

1. INTRODUCTION

Accreting massive black holes at galaxy centers are called active galactic nuclei (AGN), the brightest of which are known as quasars (QSOs), which vastly outshine their host galaxies. AGN and QSOs are classified into two types based on their spectral features: broad-line type 1 QSOs (QSO1s, unobscured black hole), and narrow-line type 2 QSOs (QSO2s, obscured black hole). There have been two

leading theories for the relationship between QSO1s and QSO2s. The orientation theory (e.g., Antonucci 1993) postulates that QSO1s and QSO2s both contain dusty tori, but are viewed at different orientations.

The other theory postulates an evolutionary scenario, where mergers give rise to QSO2s which then evolve into QSO1s (e.g., Hopkins et al. 2008b; Alexander & Hickox 2012). This theory is based on the fact that some quasar activity can be triggered by gas-rich mergers (e.g., Sanders et al. 1988a,b; Sanders & Mirabel 1996; Urrutia et al. 2008; Petric et al. 2011; Glikman et al. 2015; Ellison et al. 2019). At higher redshift ($z \gtrsim 1$), studies have discovered that

the farthest, most luminous, and dustiest of QSOs¹ bear the marks of gravitational interactions from tidal tails to complex nuclear structures² (e.g., Urrutia et al. 2008; Glikman et al. 2012, 2015; Lacy et al. 2018; Kakkad et al. 2023). Urrutia et al. (2008) used the *Hubble Space Telescope* and ground-based adaptive optics to image obscured AGN to separate the emission from the nucleus and the host, and found that the hosts of obscured AGN tend to be major mergers. The observations in Glikman et al. (2012, 2015) are particularly telling: at the peak epoch for galaxy and black hole growth, the most luminous QSOs are also the most dust reddened, and their host galaxies are major mergers. These observations along with simulations (e.g., Hopkins et al. 2006) prompt the evolutionary link between mergers, QSO2s, and QSO1s: the merger and associated starburst stir up the gas and dust near the black hole, triggering quasar activity that gives rise to QSO2s; the black hole emerges as QSO1s only when its winds and UV emission clear the obscuring dust and gas from the nuclear region, e.g., in a “blow-out phase” (see Fig.1 in Hopkins et al. 2006). This evolutionary scenario predicts a decrease in the gas fraction from mergers to QSO2s and then to QSO1s. If AGN produce negative feedback on the star formation (SF) of the host galaxies, the star-formation efficiency (SFE) is also expected to decrease from mergers to QSO1s.

At $z \leq 0.5$ some QSO2s are consistent with being differently oriented QSO1s expected from traditional, orientation-based unification models (e.g., Zakamska et al. 2005), while other QSO2s appear to be intrinsically different. Relative to QSO1s, these QSO2s which appear to be intrinsically different seem to have higher star formation rates (SFR; e.g., Kim et al. 2006; Lacy et al. 2007; Zakamska et al. 2008) and more chaotic ionized gas velocity fields (e.g., Greene et al. 2011). These properties are qualitatively consistent with these QSO2s being the evolutionary precursors to QSO1s, formed during the turbulent aftermath of gas-rich mergers.

As many as $\sim 90\%$ of nearby luminous infrared galaxies (LIRGs) are gas-rich mergers (e.g., Stierwalt et al. 2013; Larson et al. 2016; Petric et al. 2018). Gas-rich mergers in general and LIRGs, in particular, have been proposed as precursors of QSOs (Sanders et al. 1988a,b; Sanders & Mirabel 1996; Hopkins et al. 2008a). A progression from gas-rich mergers (e.g., LIRGs) to QSO2s would imply higher gas fractions in LIRGs relative to QSO2s. If feedback from the AGN effectively impacts the molecular gas and hence the host galaxy’s ability to make new stars, we would expect QSO1s to have lower gas fractions and SFE than QSO2s. Therefore, comparing the interstellar medium (ISM) in LIRGs, QSO2s, and QSO1s can provide valuable insights

into the evolutionary link between them. As the second most abundant molecule in space, CO via observations of its $J = 1-0$ line in emission has traditionally been used as a molecular gas tracer and in turn used to infer the total H_2 gas mass in both the Milky Way and external galaxies (e.g., Bolatto et al. 2013). However, there is increasing evidence for the existence of molecular gas not traced by CO (Grenier et al. 2005), the “CO-dark” H_2 . The properties of the CO-dark H_2 gas have been widely studied via both observations of the [C II] emission (Pineda et al. 2013; Madden et al. 2013; Hall et al. 2020; Fadda et al. 2021; Liszt & Gerin 2023) and simulations (e.g., Li et al. 2018).

The [C II] $158\mu\text{m}$ fine structure line of singly ionized carbon is one of the major coolants of neutral gas in the ISM and photodissociation regions (PDRs; Wolfire et al. 2003; Narayanan & Krumholz 2016). The [C II] emission primarily arises as a result of FUV radiation from O and B stars ionizing carbon in the molecular clouds of PDRs. While the abundance of carbon is predominantly locked into CO in dense regions of molecular clouds that are well-shielded from FUV radiation, the [C II] emission arises from multiple layers of PDRs but most likely originates from the outer, more diffuse gas layers with overall lower molecular fractions. Thus [C II] provides a complementary probe of the ISM to CO which traces denser gas that is physically related to star formation (Narayanan & Krumholz 2016; Garcia et al. 2023) and has the potential of providing additional insights on ISM conditions not accessible to CO observations alone.

In this paper, we present observations of the CO(1–0) and (2–1) lines using the Institut de radioastronomie millimétrique (IRAM) 30m telescope for 20 nearby, optically luminous QSO2s that have existing FIR observations from the *Herschel Space Observatory* (Pilbratt et al. 2010). We also present [C II] $158\mu\text{m}$ observations from the Stratospheric Observatory For Infrared Astronomy (SOFIA; Young et al. 2012), of unprecedented sensitivity, for 5 QSO2s from the CO sample as well as for 5 QSO1s from the Palomar–Green (PG) bright quasar survey (Schmidt & Green 1983; Boroson & Green 1992). Combined with observations of nearby LIRGs (e.g., the Great Observatories All-sky Survey, Armus et al. 2009) from the literature, our data permits a meaningful comparison in the CO and [C II] observations of local QSOs and LIRGs. In addition, the SOFIA data will assess the utility of the [C II] cooling line as a SF tracer compared to other tracers such as the CO and FIR luminosity. Given the scarcity of CO and [C II] observations of nearby QSOs for which we have optical spectroscopy, our data form the basis for a benchmark sample of nearby QSOs to compare with QSOs at higher redshifts.

AGN are believed to dramatically affect the gas within their hosts and play an important role in suppressing SF (e.g., Kakkad et al. 2017). Yet direct observational evi-

¹ Hereafter QSOs refer to their host galaxies.

² Although see Villforth et al. (2017) for a counter-argument.

dence for AGN quenching remains somewhat elusive. Multi-wavelength studies of AGN are necessary to gain a more comprehensive understanding of the effects of AGN on their host environments. The galaxies in our sample are chosen specifically to have data across multiple wavelengths from the mid-infrared (MIR) to the far-infrared (FIR) regimes. The combination of our data with archival data sets will help compare the physical properties of the ISM (e.g., molecular gas mass M_{H_2} and molecular gas fraction M_{H_2}/M_*) and SFE between QSO1s, QSO2s, and LIRGs, with the aim of gleaning a more global understanding of how the ISM conditions differ in different types of QSOs and shed light on the evolutionary link between QSOs and LIRGs.

This paper is organized as follows. We present our sample selection and observation details in §2. The results of our observations (detection of molecular gas and derived physical quantities) are presented in §3. We compare observed and derived ISM properties across different samples and explore the implications of our study in §4. We summarize our conclusions in §5 and provide ancillary data gathered from the literature in §6. Throughout this paper we assume the cosmological parameters $H_0 = 70 \text{ km s}^{-1} \text{ Mpc}^{-1}$, $\Omega_m = 0.3$, and $\Omega_\Lambda = 0.7$.

2. SAMPLE AND DATA

Shangguan & Ho (2019) selected 87 QSO2s from the Sloan Digital Sky Survey (SDSS; Reyes et al. 2008) that match the PG QSO1s in both redshift and [O III] $\lambda 5007$ luminosity (Fig.1 in Shangguan & Ho 2019, see also Petric et al. 2015; Zakamska et al. 2016). Both samples of QSO2s and QSO1s satisfy the historical criterion of $M_B < -23$ mag for quasars (Schmidt & Green 1983), representing the extremely luminous end of accreting black holes. These closely matched QSO2s and QSO1s make an excellent sample for studying the differences in the ISM properties between the two types of QSOs. To obtain information on the ISM, we select the 20 most nearby QSO2s from Shangguan & Ho (2019) to observe with IRAM for CO emission. We also select the 5 nearest QSO2s from our CO sample and the 5 nearest PG QSO1s observable within the SOFIA atmospheric window for [C II] observations. A complete list of our targets and observations are tabulated in Table 1, 2, and 3. Details about our observations and data reduction are presented in the following sections.

2.1. IRAM CO Observations and Data Reduction

We observe our sample of QSO2s with the IRAM 30m telescope, in Pico Veleta, Spain, during two observation periods: 14–20 August 2012 and 8–10 January 2013 (PI: Petric). The Eight MIXer Receiver (EMIR) instrument was used in wobbler switching mode with a reference position offset of $120''$ at a frequency of 1 Hz or 0.8 Hz. We take advantage

of the 32 GHz wide available bandwidth to simultaneously observe the CO(1–0) and CO(2–1) using the E090 and E230 EMIR bands with the Wideband Line Multiple Autocorrelator (WILMA) backend.

The CO(1–0) line is anticipated at $106.153 \leq \nu_{\text{CO}(1-0)} \leq 111.158$ GHz and the CO(2–1) line $212.301 \leq \nu_{\text{CO}(2-1)} \leq 222.312$ GHz at our targets' optical redshifts. Local oscillator (LO) frequencies were chosen to place the CO(1–0) of multiple targets in the Upper Inner sideband of EMIR. This reduces the overheads to 1 or 2 LO tunings per 12 hours of observation. The anticipated CO line was kept at least 400 MHz from the band edge to allow for base-lining. We take the data in eight-minute scans comprised of twelve 30-second long sub-scans. Observations are interspersed with instrument calibrations every 2–3 scans and pointing calibrations every 1–2 hours on sources from the IRAM Flux Monitoring Program. Telescope refocusing is carried out approximately every 2–4 hours and following sunrise and sunset preferentially on Mars, Venus, Saturn, Jupiter, or the QSO 0316+413 (3C 84). If these were not available or very distant, bright sources from the IRAM Flux Monitoring Program were used for refocusing. SDSS10 is observed with position switching mode because we experienced problems with the wobbler switching modes.

We use the standard data reduction software, the Multi-channel Imaging and Calibration Software for Receiver Arrays (MIRA), to calibrate each science scan using the instrument calibration scan taken closest in time. The data are then reduced using the Continuum and Line Analysis Single-dish Software (CLASS³). A first-order polynomial baseline was subtracted from each individual scan. Baselines are calculated using a linear fit after exclusion of the anticipated CO-line frequencies $\frac{\nu_{\text{CO}}}{1+z} \pm 400$ MHz. All individual scans are coadded using weights based on their RMS baseline fluctuations $\sigma(T_A^*)$, although using weighting based on observation time t_{obs} gives negligible changes to the results ($\Delta\sigma(T_A^*) < 3\%$).

Following French et al. (2015), line intensities are estimated by summing over the line profile at velocities $v_0 \pm 3\sigma(v)$, where v_0 and $\sigma(v)$ are the mean and standard deviation of a Gaussian profile fit to the CO line intensity I_{CO} at a spectral resolution of 25 MHz. While not all lineshapes are Gaussian, this method estimates an appropriate integration interval systematically. We calculate the error in the integrated CO line intensity as

$$\sigma_I^2 = (\Delta v)^2 \sigma^2 N_l \left(1 + \frac{N_b}{N_l} \right), \quad (1)$$

³ Part of the GILDAS software package <https://www.iram.fr/IRAMFR/GILDAS/>.

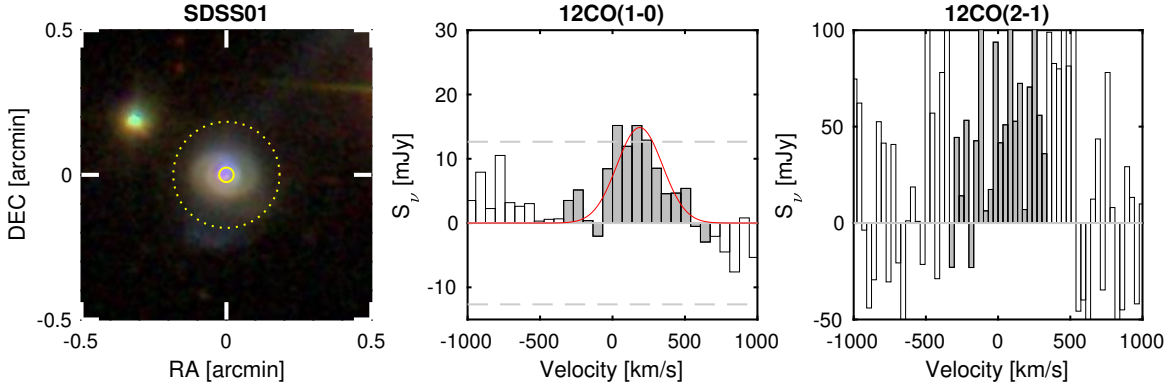


Figure 1. **Left:** $60'' \times 60''$ SDSS (*gri*) cutouts of the QSO2s. The solid and dotted yellow circles show the extent of the $3''$ SDSS spectroscopy fiber and the $22''$ IRAM beam at 3 mm, respectively. **Middle:** CO(1–0) spectra in units of mJy. **Right:** CO(2–1) spectra in units of mJy. For both spectra, the x-axis indicates the velocity offset of the line from the systemic velocity of the galaxy as determined by the optical spectrum. Spectra are shown at 25 MHz resolution and were taken from the WILMA backend. The dark grey shaded area indicates the CO line region used for the determination of I_{CO} and the red line is the Gaussian fit. Horizontal grey lines indicate the baseline (solid) and the 3σ scatter around the baseline (dashed). The complete figure set (20 images) is available in the online journal.

where $\Delta v = 71$ km/s is the channel velocity width, σ is the channel RMS noise, N_l the number of channels used to integrate over the CO-line, and N_b the number of channels used to fit the baseline (typically 32). We also take into account an estimated flux calibration error of 10%. For non-detections, we calculate upper limits on I_{CO} as $< 3\sigma_I$.

From the line intensity (I_{CO} in K km/s pc 2)⁴ we calculate the CO line luminosity L'_{CO} (in K km/s pc 2) following (Solomon et al. 1997)

$$L'_{\text{CO}} = 23.5 \Omega_{s*b} D_L^2 I_{\text{CO}} (1+z)^{-3}, \quad (2)$$

where z is the redshift from Reyes et al. (2008) and D_L is the corresponding luminosity distance in Mpc. Ω_{s*b} is the solid angle of the source convolved with the beam:

$$\Omega_{s*b} = \frac{\pi(\theta_s^2 + \theta_b^2)}{4 \ln(2)}, \quad (3)$$

where θ_s and θ_b are the half-power beam widths of the source and beam, respectively. Given the size of our sources with respect to θ_b (see Fig.1), we assume that the beam is much larger than the source size, i.e., $\Omega_{s*b} \approx \Omega_b$. The final spectra of our observed sources alongside image cutouts from SDSS are shown in Fig.1. The derived CO luminosities are summarized in Tables 1 and 2.

2.2. SOFIA [C II] Observations and Data Reduction

The SOFIA Far Infrared Field-Imaging Line Spectrometer (FIFI-LS; Fischer et al. 2018; Colditz et al. 2018) observations presented here are observed during multiple flights scheduled across multiple campaigns between August 2020

and February 2023 with one-hour on-source integration except for the FIR luminous QSO1 UGC 05025, for which the total on-source integration is only 30 minutes. We use symmetric chop nodding centering the red channel of FIFI-LS on the [C II] $158\mu\text{m}$ line. We center the blue channel on the [O III] $88\mu\text{m}$ line when it does not coincide with telluric features. Several sources are observed in multiple observing runs due to weather or technical issues.

The raw data are downloaded and reduced using the FIFI-LS pipeline (Vacca et al. 2020) and the latest calibration described in Fadda et al. (2023b). The reduction includes flagging bad pixels, removing scans affected by bad pointings or bad atmospheric transmission, and correcting for the atmospheric absorption using precipitated water vapor values evaluated during the flights (see Iserlohe et al. 2021). In particular, for lines close to a broad telluric absorption line, we apply the atmospheric transmission correction at the center of the line to avoid overcorrecting the line wings.

We then use the SOFIA package SOSPEX (Fadda & Chambers 2018) to fit the [C II] $158\mu\text{m}$ and [O III] $88\mu\text{m}$ lines within an aperture corresponding to the PSF FWHM at the line wavelengths ($8.8''$ and $15.2''$ diameter for [O III] $88\mu\text{m}$ and [C II] $158\mu\text{m}$, respectively) and estimate their intensities. In the case of extended emission, we also measure [C II] $158\mu\text{m}$ emission across the host galaxy. Our flux measurements are summarized in Table 3 and the [C II] spectra are shown in Fig.2.

2.3. Reference Samples from the Literature

To explore the evolutionary link between LIRGs, QSO2s, and QSO1s, we select samples of local LIRGs and QSO1s with all CO or [C II], FIR, and stellar mass (M_*) measurements, to compare with our CO and [C II] observations of local QSOs. We explain in the following paragraphs how we select our comparison samples and summarize the different

⁴ I_{CO} and L'_{CO} are computed assuming the main-beam temperature $T_{\text{mb}} = 1.33T_A^*$ on <https://www.iram.fr/IRAMFR/ARN/jan95/node46.html>.

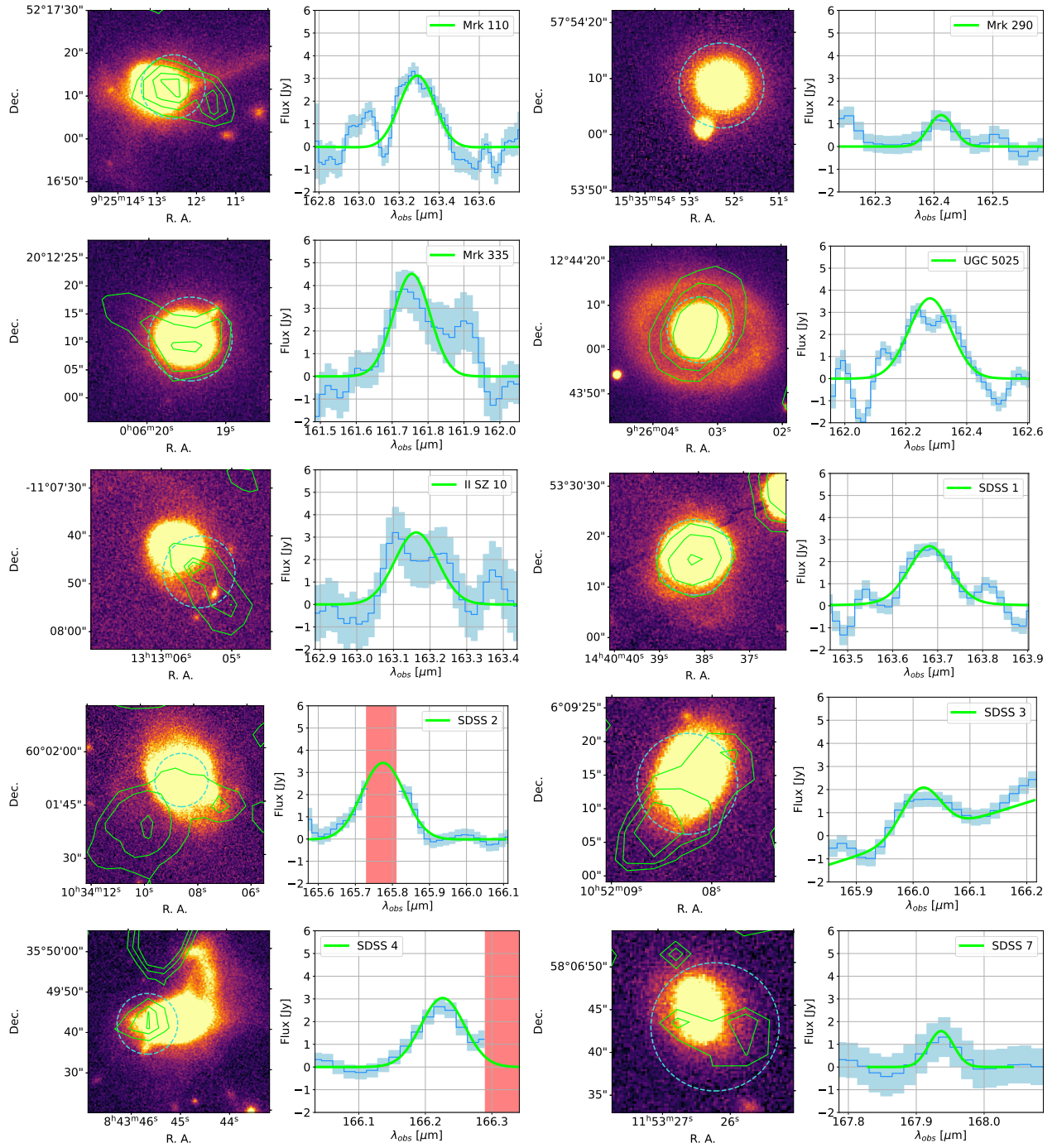


Figure 2. [C II] observations from SOFIA/FIFI-LS. Contours (solid lines) of the total [C II] intensity are overlaid on PanSTARRS *i*-band images. The aperture (dashed circle) used to extract the spectrum has a diameter of 15.2'', corresponding to the FWHM of the FIFI-LS beam at this frequency. Spectra and their 3- σ errors are shown as a blue line and a light blue band. The red vertical band in the spectra indicates the masked region due to strong atmospheric absorption. The green curves correspond to the fits of the [C II] lines.

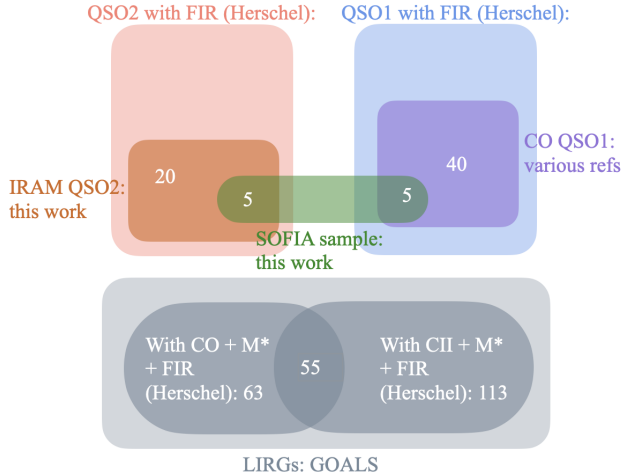


Figure 3. The Venn diagram summarizing the different samples used in this work.

data sets with a Venn diagram in Fig.3. For our QSO2 sample (SDSS02–SDSS20), we obtain M_* and FIR data from Shangguan & Ho (2019). The M_* for SDSS01 is taken from Koss et al. (2011) and the FIR data is from Meléndez et al. (2014).

The LIRGs for comparison are from the Great Observatories All-sky LIRG Survey (GOALS; Armus et al. 2009). GOALS galaxies contain mergers which could be the trigger of obscured AGN activity as suggested by the evolutionary scenario, although the luminosities of GOALS galaxies are dominated by SF, with $\lesssim 10\%$ GOALS galaxies having AGN bolometric contribution to the infrared luminosities $\gtrsim 25\%$ (e.g., Petric et al. 2011; Alonso-Herrero et al. 2012; Díaz-Santos et al. 2017). Our sample of QSOs is selected to be extremely bright (§2) and thus despite possible small overlap with GOALS galaxies containing AGN, they should represent different populations of galaxies and provide informative comparison as possible different evolutionary stages. We construct the CO GOALS comparison sample by selecting galaxies that have 1) CO(1–0) measurements in Yamashita et al. (2017) or Herrero-Illana et al. (2019)⁵ 2) FIR measurements in Chu et al. (2017) 3) M_* estimates in Howell et al. (2010). For the [C II] GOALS comparison sample, we use the same sources for FIR and M_* , but select those galaxies with [C II] measurements presented in Díaz-Santos et al. (2017)⁶. We end up with 63 CO GOALS galaxies and 113 [C II] GOALS galaxies.

For the CO QSO1 comparison sample, we select from the PG quasars that roughly match our IRAM QSO2s in red-

⁵ For GOALS galaxies in both Yamashita et al. (2017) and Herrero-Illana et al. (2019), we use the measurements from Herrero-Illana et al. (2019) because their observations were also from the IRAM 30m telescope.

⁶ We use their galaxy-integrated flux measured from the best aperture.

shift and [O III] $\lambda 5007$ luminosity (§2). Shangguan et al. (2020) summarized PG quasars with CO(1–0) data from the literature (Casoli & Loinard 2001; Evans et al. 2001, 2006; Bertram et al. 2007; Evans et al. 2009) in addition to presenting CO(2–1) observations of their selected PG quasars. To obtain a larger sample, we combine the CO(1–0) data converted from CO(2–1) measurements (Table 2 in Shangguan et al. 2020) and those from the literature (Table 3 and 4 in Shangguan et al. 2020). For objects with both CO(2–1)-converted and literature CO(1–0) luminosity, we adopt the more recent CO(2–1)-converted value if the literature value is an upper limit. CO(1–0) data for two additional PG quasars, PG 1534+580 and PG 0921+525, are taken from Wylezalek et al. (2022) and Salomé et al. (2023), respectively. For these QSO1s with CO data, we obtain FIR measurements from Petric et al. (2015) and M_* from Xie et al. (2021). M_* values from Xie et al. (2021) are scaled to the stellar initial mass function (IMF) of Salpeter (1955). We divide these M_* values by 1.5 to convert them to the Chabrier (2003) IMF to be consistent with the M_* of GOALS galaxies and QSO2s.

The FIR observations for our samples of LIRGs, QSO1s, and QSO2s are from *Herschel*. We use $160\mu\text{m}$ photometry because data at this wavelength, the longest observable wavelength of the Photodetector Array Camera and Spectrometer (PACS), are available for all samples. Emission at $160\mu\text{m}$ traces the coldest dust observable with PACS and they are not as impacted by confusion as longer wavelength observations with the Spectral and Photometric Imaging Receiver (SPIRE) because PACS data have higher spatial resolution than SPIRE. The $160\mu\text{m}$ fluxes obtained from the literature as described above have been corrected for aperture effects in corresponding works and represent the integrated flux for the entire galaxy. We convert observed fluxes at $160\mu\text{m}$ to rest-frame luminosities assuming a flat spectral shape around $160\mu\text{m}$. This is a reasonable assumption based on existing spectral energy distribution (SED) analysis on our galaxies (e.g., U et al. 2012; Petric et al. 2015; Shangguan et al. 2019; Shangguan & Ho 2019; Paspaliaris et al. 2021). We determine $F_{\lambda_{\text{rest}}}$ from observed fluxes using $\lambda_{\text{rest}} = \lambda_{\text{obs}}/(1+z)$, and derive the spectral index ($\alpha : F_{\lambda} \propto \lambda^{\alpha}$) from observed fluxes at $100\mu\text{m}$ ⁷ and $160\mu\text{m}$. The final luminosity at rest-frame $160\mu\text{m}$ is estimated using the spectral index.

The data we obtain from the literature are summarized in §6. The M_* distributions of our samples are similar (e.g., Fig.4 and Fig.5). Since our samples of LIRGs, QSO1s, and QSO2s are all nearby, our comparison of ISM properties between the samples should not be affected by redshift or M_* . We elaborate on the results of our comparison in §4.1.

3. RESULTS

⁷ When fluxes at $100\mu\text{m}$ are not available, we use fluxes at $70\mu\text{m}$.

3.1. Detection of CO in QSO2s

As shown in Table 1 and 2, we robustly detect CO molecular gas emission in the CO(1–0) line in 50% of the 20 optically luminous QSO2s with a minimum detection limit of $0.4 \pm 0.1 \text{ K km s}^{-1}$ and the brightest CO(1–0) emission at $1.2 \pm 0.2 \text{ K km s}^{-1}$. Whether a source is detected is determined based on both the signal level above the continuum and the likelihood that a set of channels will have enhanced emission at the expected line frequency. The flux uncertainty estimation is described in §2.1. The $I_{\text{CO}(1-0)}$ upper limits range between 0.4 and 1.1 K km s^{-1} and the median $I_{\text{CO}(1-0)}$ of the detected sources is 0.8 K km s^{-1} .

We detect CO(2–1) in 40% of the 15 QSO2s we target in this line. The faintest and brightest detections are 0.4 ± 0.2 and $2.5 \pm 0.4 \text{ K km s}^{-1}$. The $I_{\text{CO}(2-1)}$ upper limits range between 0.3 and 3.1 K km s^{-1} and the median $I_{\text{CO}(2-1)}$ of the detected sources is 1.3 K km s^{-1} .

Toward 4 sources we have robust detection of both the CO(1–0) and CO(2–1) emission while 2 sources have CO(2–1) measurements but not CO(1–0). We compute the line ratio $R_{21} = \frac{L'_{\text{CO}(2-1)}}{L'_{\text{CO}(1-0)}}$ for the 4 QSO2s with both lines detected and the values are recorded in Table 1 and 2. The R_{21} values for our QSO2s span a wide range of 0.45–1.35 which is roughly in agreement with the range of 0.49–0.90 found for PG QSO1s in Shangguan et al. (2020). Our median R_{21} is 0.82 and we use this value to estimate the CO(1–0) luminosity of the 2 QSO2s that only have CO(2–1) measurements.

3.2. Detection of [C II] in QSO1s and QSO2s

We robustly detect [C II] $158\mu\text{m}$ emission in all 5 QSO2s and 4/5 QSO1s. The measured [C II] fluxes are summarized in Table 3 and we provide the upper limit on [C II] flux for the QSO1 toward which we do not detect [C II] emission. The [O III] $88\mu\text{m}$ line is observed in parallel for 6 QSOs and 4 of them are detected in this line. We provide [O III] $88\mu\text{m}$ fluxes for these detected sources. The uncertainties in the flux measurements for both lines are predominantly calibration errors, which we adopt to be 15%⁸ of the reported fluxes.

3 QSO1s and 3 QSO2s have extended [C II] $158\mu\text{m}$ emission. For those sources, the total flux which is larger than the flux enclosed in a single-resolution element is also reported in Table 3.

4. DISCUSSION

4.1. Comparison between Nearby LIRGs, QSO2s, and QSO1s

4.1.1. CO

We plot the CO, FIR, and M_* data for our samples in Fig.4. To compare the distributions of different physical quantities across samples, we derive cumulative distributions of different physical quantities and perform two-sample statistical tests using the Python package `lifelines`⁹. Given that the data contains upper limits (left-censored data), the cumulative distributions are based on the Kaplan–Meier estimator (Kaplan & Meier 1958), and the two-sample tests we use here are the Logrank test, Peto–Peto test, Wilcoxon test, and Tarone–Ware test (Feigelson & Nelson 1985; Feigelson & Babu 2012).

The cumulative distributions of L'_{CO} , $L_{160\mu\text{m}}$, $L'_{\text{CO}}/L_{160\mu\text{m}}$, and M_* for QSO1s, QSO2s, and LIRGs are shown in Fig.5 and the test results are summarized in Table 4. The test statistics represent how different the two samples are, and the p -values represent the likelihood that the two samples arise from the same underlying distribution (the smaller the p -value the less likely). We adopt here a conservative threshold that $p < 10^{-3}$ indicates that the two samples are from distinctive distributions while $p > 0.1$ indicates that the two samples are statistically indistinguishable. p -values in between imply marginal differences between the two samples and we interpret them as possible hints for future analysis.

QSO1s and QSO2s appear statistically indistinguishable in all four physical quantities. When compared to LIRGs which are hypothesized to be the precursors of both QSO1s and QSO2s, both types of QSOs show different distributions from LIRGs in CO and FIR luminosity, with LIRGs showing larger values of L'_{CO} and $L_{160\mu\text{m}}$. This result is not unexpected as LIRGs are IR-luminous by definition. Both higher L'_{CO} and $L_{160\mu\text{m}}$ suggest that there is more SF activity in LIRGs than in QSOs, which is consistent with the evolutionary scenario. However, all three samples have statistically indistinguishable distributions for $L'_{\text{CO}}/L_{160\mu\text{m}}$ and M_* . $L'_{\text{CO}}/L_{160\mu\text{m}}$ is an indicator of the SFE since the numerator and denominator trace the SF fuel available and ongoing SF, respectively. The tight linear correlation between CO and FIR luminosities (upper left panel of Fig.4) implies that FIR emission in our samples is mainly from dust heated by star formation rather than by AGN (see also Petric et al. 2011; Zakamska et al. 2016; Shangguan et al. 2020). Therefore, despite showing more SF activity, the LIRGs in our sample are forming stars at the same efficiency as QSO1s and QSO2s. The similar distribution for M_* ensures that the differences/similarities we observe in our samples are not affected by M_* .

To test for systematic differences between the ISM content of LIRGs, QSO2s, and QSO1s, we relate CO observations

⁸ 25% for IISZ010 due to higher background uncertainty.

⁹ <https://lifelines.readthedocs.io/en/latest/>

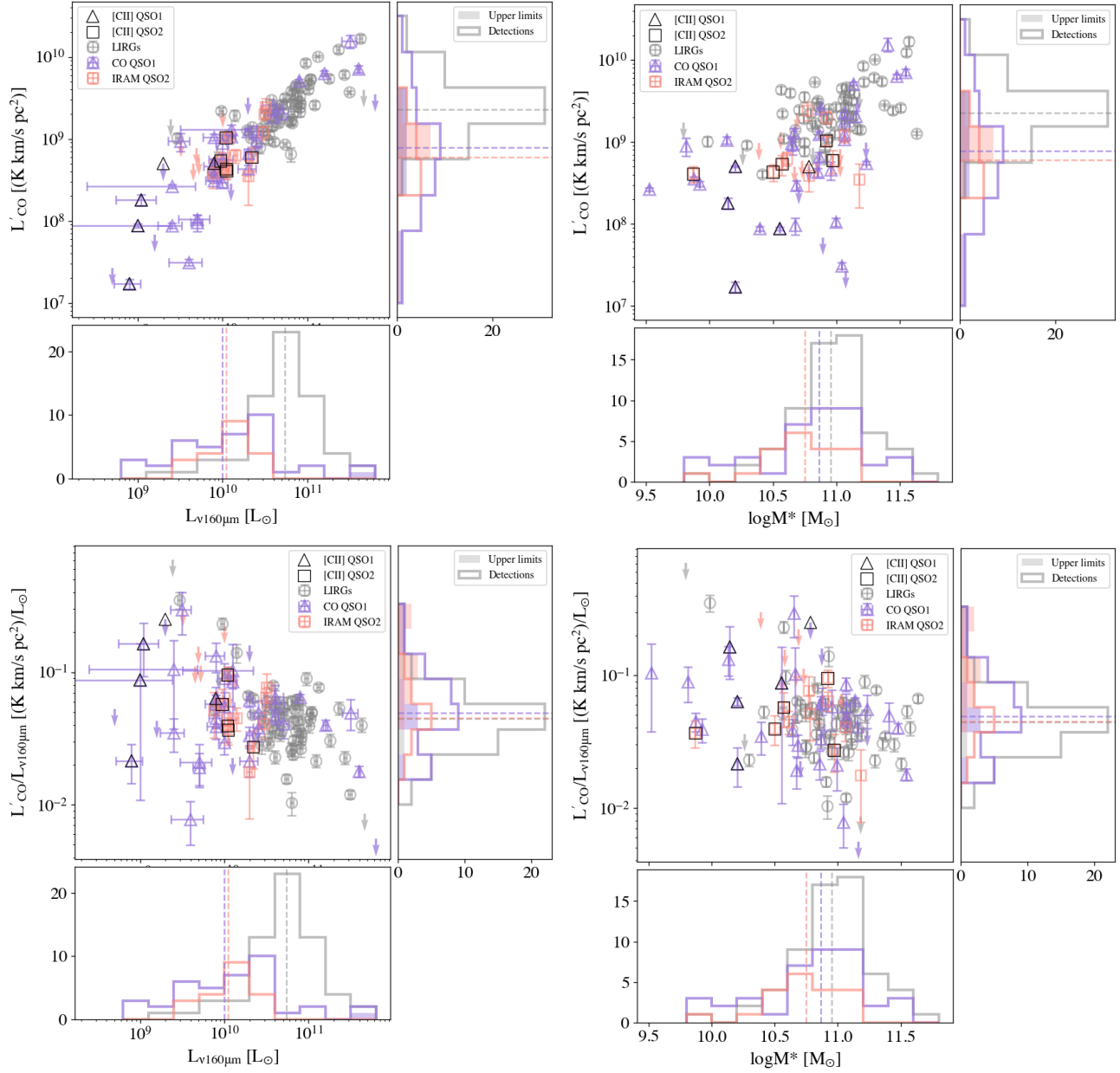


Figure 4. **Upper left:** CO(1–0) luminosity versus FIR luminosity at $160\mu\text{m}$. **Upper right:** CO(1–0) luminosity versus galaxy stellar mass. **Lower left:** CO over FIR luminosity ratio versus FIR luminosity at $160\mu\text{m}$. **Lower right:** CO over FIR luminosity ratio versus galaxy stellar mass. Upper limits are indicated by downward arrows. Dashed lines at the histograms indicate the median of detected values. Values obtained from the literature are detailed in §2.3 and summarized in Table 5, 6, and 7. QSOs with [C II] data available in this paper are indicated by additional black markers.

to ISM content by deriving the molecular gas mass (M_{H_2}) and gas fraction (M_{H_2}/M_*) for our samples. For consistency, we use M_{H_2} derived from the CO-to- H_2 conversion factor (α_{CO}): $M_{\text{H}_2, \text{CO}} = \alpha_{\text{CO}} \times L'_{\text{CO}}$. We choose the most suitable value of α_{CO} for each of our samples, based on the literature: $\alpha_{\text{CO, QSO1}} = 3.1 \text{ (K km s}^{-1} \text{pc}^2)^{-1}$ for QSO1s (Shangguan et al. 2020), $\alpha_{\text{CO, QSO2}} = 4.3 \text{ (K km s}^{-1} \text{pc}^2)^{-1}$ for QSO2s (Ramos Almeida et al. 2022), and $\alpha_{\text{CO, LIRG}} = 1.8 \text{ (K km}$

$\text{s}^{-1} \text{pc}^2)^{-1}$ for LIRGs (Herrero-Illana et al. 2019; Montoya Arroyave et al. 2023).

We plot the cumulative distributions of $M_{\text{H}_2, \text{CO}}$ and $M_{\text{H}_2, \text{CO}}/M_*$ in Fig.6 and record the two-sample statistical test results in Table 4. QSO1s and QSO2s show statistically indistinguishable distributions for $M_{\text{H}_2, \text{CO}}$ and $M_{\text{H}_2, \text{CO}}/M_*$. Based on the test statistics (Table 4), LIRGs appear to have similar $M_{\text{H}_2, \text{CO}}$ distribution and identical $M_{\text{H}_2, \text{CO}}/M_*$ distribution as QSO2s, but display relatively larger differences

compared to QSO1s in both quantities (LIRGs show larger $M_{\text{H}_2, \text{CO}}$ and $M_{\text{H}_2, \text{CO}}/M_*$). Although LIRGs tend to have brighter CO emission than QSO2s (Fig.4 and 5), they have similar gas fractions and thus similar molecular gas reservoirs. We note that α_{CO} is known to be uncertain and can even vary within a single galaxy (e.g., Bolatto et al. 2013). Although LIRGs show larger L'_{CO} than QSOs, they are known to have smaller α_{CO} due to complex gas dynamics from mergers (Bolatto et al. 2013 and references therein). The $\alpha_{\text{CO, LIRG}}$ adopted here are tested against other molecular gas estimators (Herrero-Illana et al. 2019; Montoya Arroyave et al. 2023) and the similarity of molecular gas content in the two types of QSOs agrees with previous findings in the literature (e.g., Krips et al. 2012; Villar-Martín et al. 2013). To study the ISM content of our samples from a different perspective, we carry out a similar comparison using [C II] as a proxy for ISM gas in the following section.

4.1.2. [C II]

The relation between [C II] and FIR luminosity has been frequently used to probe the gas and dust content in high redshift galaxies (e.g., Carilli & Walter 2013). We plot L_{CII}^{10} versus $L_{160\mu\text{m}}$ in Fig.7. The LIRGs are color-coded by the fractional contribution of AGN to MIR luminosity (AGN fractions) derived from multiple MIR diagnostics as described in §4.1 of Petric et al. (2011). We observe the expected correlation between L_{CII} and $L_{160\mu\text{m}}$ in our samples and fit a line to the LIRGs with AGN fractions less than 0.2. The QSOs also follow the correlation demonstrated by the line fit, though the QSO1s display more scatter. The slope of this line is less than 1, which indicates some “deficit” in the [C II] line emission compared to the underlying dust continuum emission. In Fig.8 we plot the luminosity ratio between [C II] and FIR versus M_* and FIR luminosity. While we use the luminosity at $160\mu\text{m}$ instead of the total FIR luminosity, we observe in the right panel of Fig.8 the negative trend between $L_{\text{CII}}/L_{160\mu\text{m}}$ and $L_{160\mu\text{m}}$ with LIRG AGN spanning the whole y-axis range as reported in Díaz-Santos et al. (2013). QSO1s tend to show larger [C II]/FIR compared to LIRGs and QSO2s. In the left panel of Fig.8, the [C II]/FIR ratio does not appear to correlate with M_* for LIRGs and QSO2s, but seems to decrease with M_* for QSO1s.

Given its close relation with PDRs where new stars form, the [C II] luminosity has been used as a SF tracer in the literature (e.g., De Looze et al. 2014; Herrera-Camus et al. 2015; Narayanan & Krumholz 2016; Lagache et al. 2018). Here we compare our measured L_{CII} with L'_{CO} and SFRs derived from an independent indicator, the total infrared (IR) luminosity. We first convert $L_{160\mu\text{m}}$ to the total infrared luminos-

ity due to star formation using

$$\log(L_{\text{IR, SF}}[L_{\odot}]) = 1.49 + 0.90 \log(L_{160\mu\text{m}}[L_{\odot}]). \quad (4)$$

This calibration was based on star-forming galaxies as presented in Symeonidis et al. (2008). The utility of this relation on similar samples of LIRGs and their validity for QSOs are tested in Zakamska et al. (2016). We then derive the SFR using the calibration from Kennicutt (1998), adjusted to our Chabrier (2003) IMF by dividing by a factor of 1.5:

$$\text{SFR}_{\text{IR}}[M_{\odot}/\text{yr}] = 3 \times 10^{-44} L_{\text{IR}}[\text{erg/s}]. \quad (5)$$

We plot SFR_{IR} versus L_{CII} and SFR_{IR} versus L'_{CO} for our samples with both CO and [C II] measurements (55 LIRGs, 5 QSO1s, 5 QSO2s) in Fig.9. We observe a correlation between L_{CII} and SFR_{IR} for LIRGs and QSO2s, agreeing with the relation found in Sargsyan et al. (2012) on a sample of starburst and AGN host galaxies. We find that QSO1s lie below this relation formed by LIRGs and QSO2s, but follow the L'_{CO} -SFR correlation formed by LIRGs and QSO2s, a trend also seen in the L'_{CO} versus $L_{160\mu\text{m}}$ plot with all samples that have CO data (upper left panel of Fig.4).

We further compare L'_{CO} , L_{CII} , and SFR in our samples by plotting $L'_{\text{CO}}/L_{\text{CII}}$ versus SFR_{IR} in Fig.10. The H_2 mass could also be derived from L_{CII} : $M_{\text{H}_2, \text{CII}} = \alpha_{\text{CII}} \times L_{\text{CII}}$ (e.g., Zanella et al. 2018; Madden et al. 2020). If CO and [C II] are tracing the same gas in galaxies, i.e., $M_{\text{H}_2, \text{CO}} = M_{\text{H}_2, \text{CII}}$, we would expect $L'_{\text{CO}}/L_{\text{CII}}$ to be the constant $\alpha_{\text{CII}}/\alpha_{\text{CO}}$. We plot in Fig.10 lines of constant $\alpha_{\text{CII}}/\alpha_{\text{CO}}$ using $\alpha_{\text{CII}} = 30 M_{\odot}/L_{\odot}$ from Zanella et al. (2018) and the α_{CO} values we used in §4.1.1. We observe that QSO1s show systematically smaller $L'_{\text{CO}}/L_{\text{CII}}$ than QSO2s and LIRGs despite a large scatter, requiring α_{CO} several times greater than the Milky Way value of $4.3 (\text{K km s}^{-1} \text{pc}^2)^{-1}$ if $M_{\text{H}_2, \text{CO}} = M_{\text{H}_2, \text{CII}}$.

Zanella et al. (2018) has tested with a heterogeneous sample including dwarf, starburst, and main-sequence galaxies that their α_{CII} is invariant with redshift, metallicity, and gas depletion time. While there are uncertainties in the α conversion factors, they are unlikely large enough to explain the low values of $L'_{\text{CO}}/L_{\text{CII}}$ shown by our sample of QSO1s. LIRGs and QSO2s show less scatter in $L'_{\text{CO}}/L_{\text{CII}}$ and are consistent with typical ranges of $\alpha_{\text{CII}}/\alpha_{\text{CO}}$ as plotted in Fig.10. This comparison of $L'_{\text{CO}}/L_{\text{CII}}$ agrees with what we observe in Fig.9: the CO emission in all three samples and the [C II] emission in QSO2s and LIRGs trace gas related to SF activity, but there seems to be an excess of [C II] emission that is unrelated to SF in some QSO1s.

In addition to molecular gas, [C II] emission also traces warm and cold neutral gas, and can be enhanced where there is an AGN (e.g., Appleton et al. 2018; Smirnova-Pinchukova et al. 2019; Fadda et al. 2021). Shocks or turbulent heating (e.g., due to mergers or ram pressure) could also lead to excess [C II] emission compared to what is expected from SF

¹⁰ We use I_{CII} for the entire galaxy, the extended emission column in Table 3 when available.

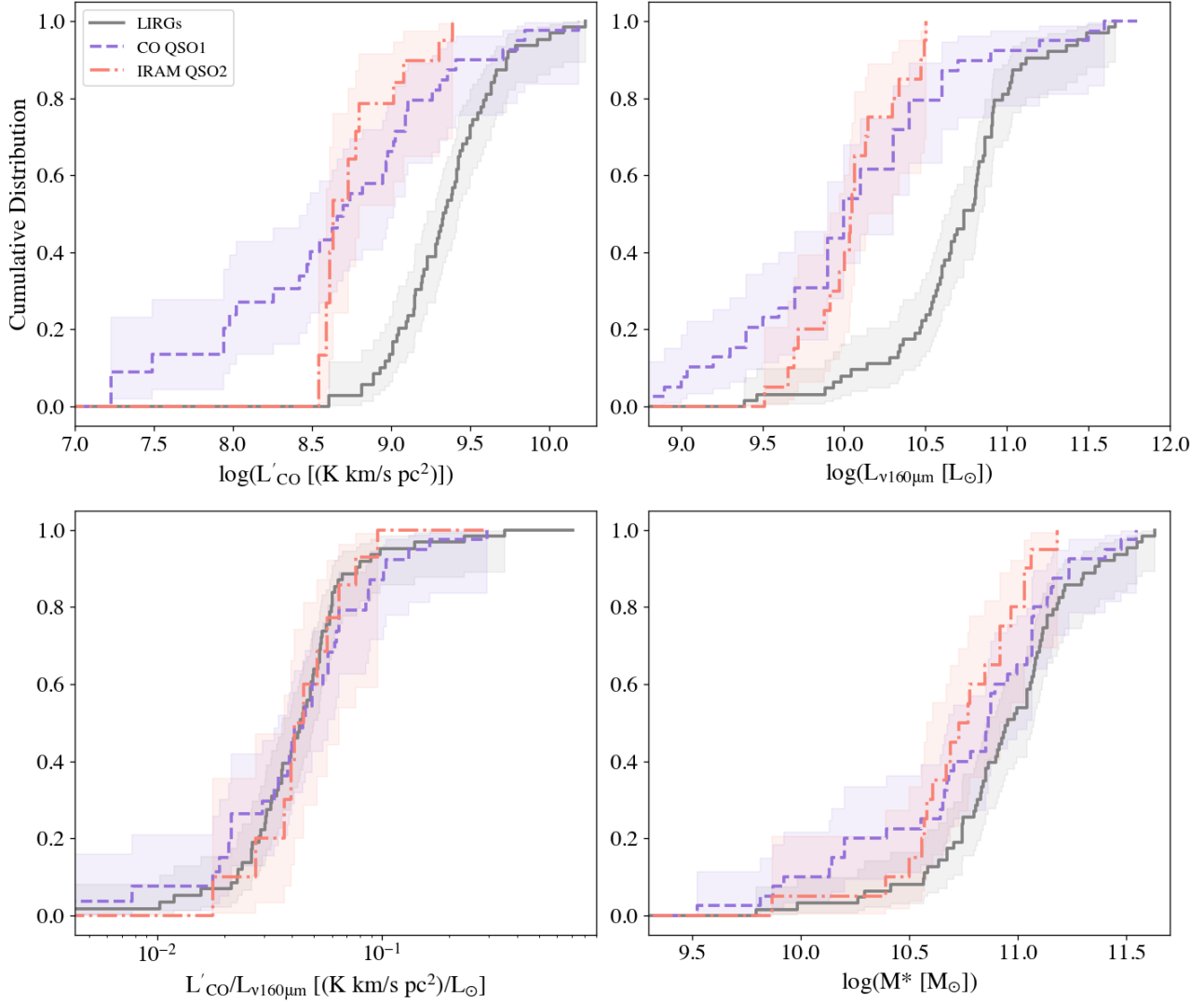


Figure 5. Cumulative distributions of CO(1–0) luminosity, FIR luminosity at $160\mu\text{m}$, the ratio of CO(1–0) over FIR luminosity, and galaxy stellar mass for our samples of LIRGs, QSO1s, and QSO2s. The distributions are derived from the Kaplan-Meier estimator taking into account undetected upper limits, and the shaded areas represent the 95% confidence intervals. Values obtained from the literature are detailed in §2.3 and summarized in Table 5, 6, and 7.

(e.g., Appleton et al. 2013; Alatalo et al. 2014; Minchin et al. 2022; Fadda et al. 2023a). LIRG, QSO1, and QSO2 samples in this work all contain galaxies showing disturbed morphology, although detailed studies on the relation between morphology and [C II] emission require higher resolution imaging data and are outside the scope of this paper. In the sample of LIRGs studied in this work, those with high AGN fractions do not have more [C II] emission than those without AGN (Fig. 7 and 8). While it is challenging to separate the effects of shocks on the observed [C II] properties in LIRGs since they are complex, gravitationally interacting, star-forming systems, the differences in [C II] emission between QSO1s and QSO2s do suggest that the multiphase ISM of these two populations differs either because of their formation history or geometric conditions. Decarli et al. (2014) found that

[C II] emission in the QSO of an interacting system arises primarily in the neutral gas and an excess of neutral gas could lead to the observed excess of [C II] emission in our SOFIA QSO1s. Furthermore, outflows can dissociate molecular gas, leading to a relatively larger fraction of ISM gas in the atomic or partially ionized phase. Black holes in the blow-out phase in QSO2s may destroy the dust and molecular gas, but the atomic gas might rain back and increase the neutral fraction of the total gas reservoirs in the QSO1 phase. Four out of five SOFIA QSO1s (except IISZ 010) also contain outflows studied in previous studies (e.g., Tombesi et al. 2010; Longinotti et al. 2019; Molina et al. 2022; Salomé et al. 2023) and these outflows might have altered their ISM content.

4.2. Implications for Origins and Evolution of QSOs

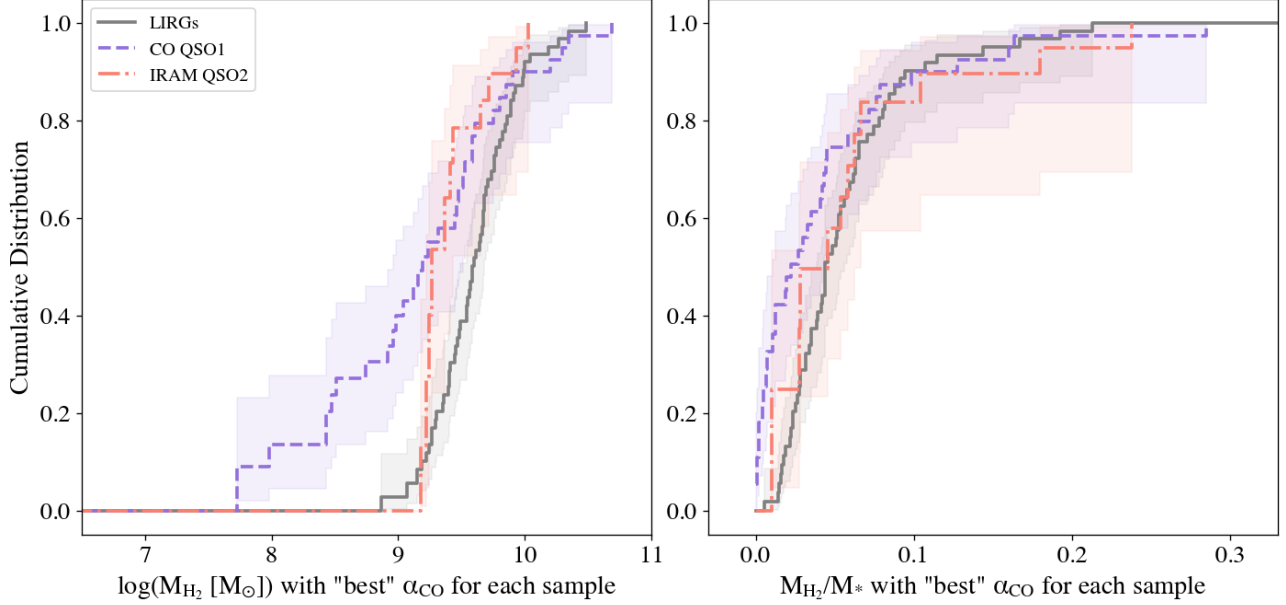


Figure 6. Cumulative distributions of $M_{\text{H}_2,\text{CO}}$ and $M_{\text{H}_2,\text{CO}}/M_*$ derived using the CO-to- H_2 conversion factor as described in §4.1.1. The distributions are derived from the Kaplan-Meier estimator taking into account undetected upper limits, and the shaded areas represent the 95% confidence intervals.

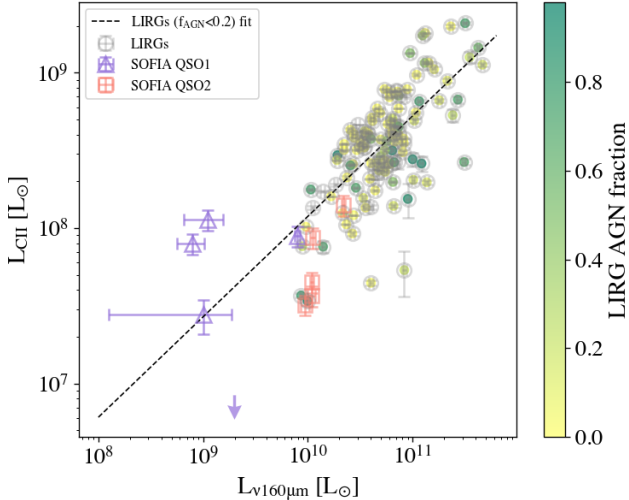


Figure 7. [C II] luminosity versus FIR luminosity at $160\mu\text{m}$. The black dashed line is fit to LIRGs with AGN fractions less than 0.2. L_{CII} and $L_{160\mu\text{m}}$ of LIRGs show the expected correlation. QSO2s lie within the scatter of LIRGs while QSO1s display more scatter.

The evolutionary picture where LIRGs evolve to QSO2s and then to QSO1s as ISM gas is removed during the black hole “blow-out” phase has been challenged when QSO1s were found to contain gas and vigorously form stars (e.g., Petric et al. 2015; Shangguan et al. 2020; Xie et al. 2021). Our comparison of the ISM content of nearby QSO1s, QSO2s, and LIRGs via observations of CO and [C II] confirms that nearby QSO2s are unlikely the precursors of nearby QSO1s but could evolve from nearby LIRGs.

LIRGs and QSO2s show similar distributions in $L'_{\text{CO}}/L_{160\mu\text{m}}$, $M_{\text{H}_2,\text{CO}}$, and $M_{\text{H}_2,\text{CO}}/M_*$ (Fig. 5, Fig. 6, Table 4), implying similar SFE and molecular gas reservoir between these two types of galaxies. Although the traditional evolutionary scenario predicts a decrease in the molecular gas fraction from mergers to QSO2s, the observed similarity from our CO data does not contradict the prediction as our sample of LIRGs contains mergers at different stages and a small fraction ($\sim 10\%$) of objects with $\gtrsim 70\%$ AGN fraction which could be the immediate predecessors of our QSO2s. The absence of a decrease in SFE might indicate that AGN do not suppress SF on the galaxy-wide scale in which our CO observations probe. In terms of [C II], QSO2s also show similarity to the LIRGs in $L_{\text{CII}}/L_{160\mu\text{m}}$ (Fig. 8) and $L'_{\text{CO}}/L_{\text{CII}}$ (Fig. 10). In Fig. 10, we notice that LIRGs with high AGN fractions show less scatter in $L'_{\text{CO}}/L_{\text{CII}}$, being more consistent with the simple model of a constant ratio between CO and [C II] luminosity. This fact could suggest that gas of different phases and metallicity are better mixed in these LIRGs so the observed CO and [C II] emission may predominantly trace the same gas reservoirs on global, galaxy-wide scales. Substantial gas mixing may occur at later stages of galaxy mergers, giving rise to luminous obscured quasars, akin to those observed in our QSO2 sample.

QSO1s, despite having similar SFE to LIRGs ($L'_{\text{CO}}/L_{160\mu\text{m}}$, lower left panels in Fig. 4 and 5), show less SF traced by $L_{160\mu\text{m}}$ and $M_{\text{H}_2,\text{CO}}$ (Fig. 5 and 6). Our results also agree with previous studies that found QSO1s and QSO2s have the same availability of molecular gas traced by CO (e.g., Krips et al. 2012; Villar-Martín et al. 2013).

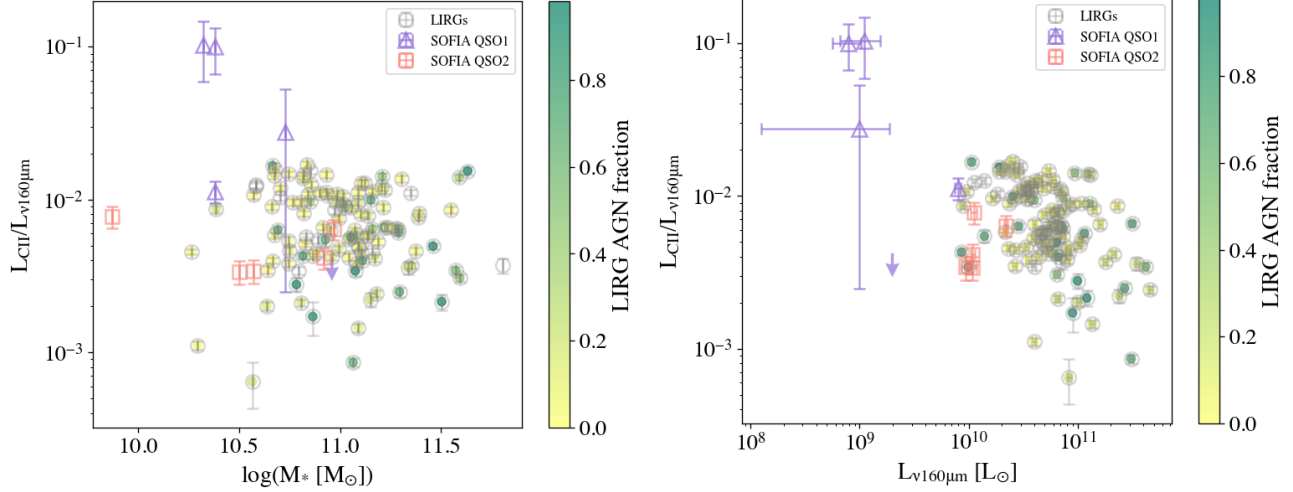


Figure 8. Left: [C II] over FIR luminosity ratio versus stellar mass. **Right:** [C II] over FIR luminosity ratio versus FIR luminosity at $160\mu\text{m}$. The LIRGs are color-coded by AGN fractions derived from multiple MIR diagnostics as described in §4.1 of [Petric et al. \(2011\)](#). Values obtained from the literature are detailed in §2.3 and summarized in Table 5, 6, and 7. QSO2s lie within the scatter of LIRGs while QSO1s display more scatter.

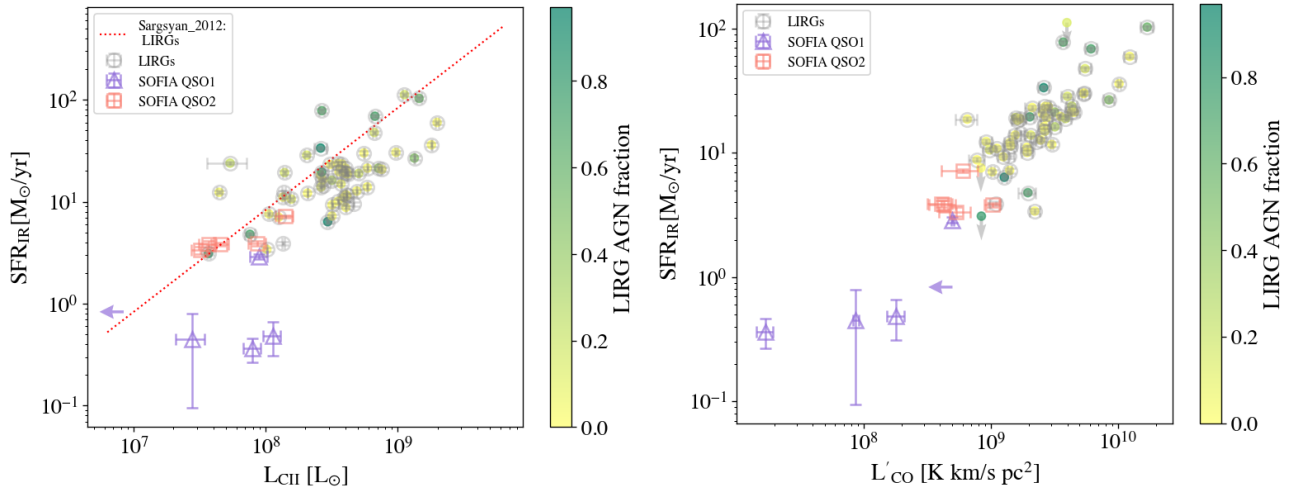


Figure 9. Left: L_{CII} versus SFR_{IR} for our samples with both CO and [C II] data. The correlation from [Sargsyan et al. \(2012\)](#) based on starburst and AGN host galaxies is overplotted. LIRGs and QSO2s agree with this correlation while most of the QSO1s lie below the correlation. **Right:** L'_{CO} versus SFR_{IR} for our samples with both CO and [C II] data. L'_{CO} in all three samples follows a tight correlation with SFR_{IR} .

Without the [C II] data, one might be under the impression that nearby QSO1s contain less gas than nearby LIRGs with similar M_* . Our finding of [C II] emission in QSO1s that does not trace SF (Fig.9 and 10) suggests that QSO1s might as well contain lots of gas with lower molecular fractions, e.g., more ionized or atomic gas. Although studies using FIR SED fitting and gas-to-dust ratios derived from galaxy stellar masses found that QSO1s and QSO2s are also indistinguishable in the total gas mass including molecular and neutral gas (e.g., [Shangguan et al. 2018](#); [Shangguan & Ho 2019](#)), future work with H I data could better constrain the total gas mass and help reveal whether QSO1s contain more total gas than QSO2s and LIRGs.

[Shangguan & Ho \(2019\)](#) found similar interstellar radiation fields in samples of QSO1s and QSO2s that contain our [C II] targets and suggested that QSO1s and QSO2s have a similar spatial distribution of ISM. The difference in L_{CII} and $L_{\text{CII}}/L_{160\mu\text{m}}$ between QSO1s and QSO2s we observe in this work might suggest otherwise. Nevertheless, analysis of larger samples combined with theoretical simulations is needed to confirm these findings ([Patil et al. in prep](#)).

The similarity of SFE, CO-, and [C II]-traced gas in our LIRGs and QSO2s, as explained above, is consistent with the hypothesis that QSO2s could emerge from gas-rich mergers like local LIRGs. The similarity of SFE and CO-traced gas between QSO2s and QSO1s, coupled with evidence of poten-

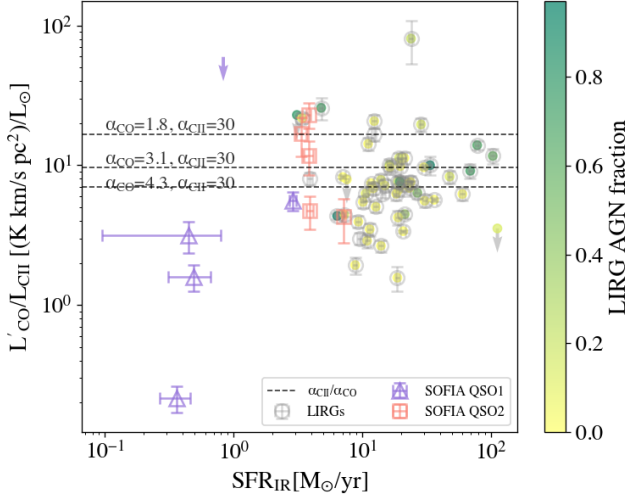


Figure 10. $L'_{\text{CO}}/L_{\text{CII}}$ versus SFR_{IR} with constant lines of $\alpha_{\text{CII}}/\alpha_{\text{CO}}$. The lines represent the case if [C II] and CO are both tracing the same gas reservoir: $\alpha_{\text{CII}} \times L_{\text{CII}} = \alpha_{\text{CO}} \times L'_{\text{CO}}$. LIRGs and QSO2s show less scatter in $L'_{\text{CO}}/L_{\text{CII}}$ and are more consistent with the constant lines. QSO1s show enhanced [C II] emission not tracing SF compared to CO emission.

tial additional gas in QSO1s from [C II] observations, does not support the evolutionary scenario that require a “blow-out” phase to remove gas to turn QSO2s to QSO1s. Our [C II] observations of QSOs also disfavor the orientation-based unification theory. Our results are consistent with previous studies (e.g., [Veilleux et al. 2009](#); [Alonso-Herrero et al. 2016](#)) which highlighted the evolutionary complexity between LIRGs and QSOs. We note that this study focuses on the low redshift universe. To better characterize the ISM gas properties and understand the time evolution of QSOs, spatially resolved observations as well as samples covering different physical properties (e.g., redshifts, masses, and merger stages) are necessary.

5. CONCLUSIONS

We present CO observations from the IRAM 30m telescope for 20 nearby, optically luminous QSO2s as well as [C II] $158\mu\text{m}$ observations from SOFIA FIFI-LS for 5 QSO2s from the CO sample and 5 PG QSO1s. Combining those data with published measurements, we compare the ISM content (M_{H_2} , M_{H_2}/M_*) and SFE (indicated by $L'_{\text{CO}}/L_{160\mu\text{m}}$) between M_* -matched QSO1s, QSO2s, and LIRGs using CO and [C II] emission as probes. Our study using direct observations of gas tracers provides valuable insights into the evolutionary link between LIRGs, QSO2s, and QSO1s in the nearby universe. Our main findings are summarized as follows:

1. QSO1s and QSO2s show statistically indistinguishable cumulative distributions in L'_{CO} , $L_{160\mu\text{m}}$, $L'_{\text{CO}}/L_{160\mu\text{m}}$, $M_{\text{H}_2,\text{CO}}$, and $M_{\text{H}_2,\text{CO}}/M_*$. The two

types of QSOs appear to have similar SFE and molecular gas reservoirs traced by CO.

2. LIRGs show larger L'_{CO} (tracing gas available for SF) and $L_{160\mu\text{m}}$ (tracing ongoing SF) than the QSOs, indicating more SF as expected. However, LIRGs show statistically indistinguishable cumulative distributions in $L'_{\text{CO}}/L_{160\mu\text{m}}$ from the QSOs, implying that QSOs are forming stars as efficiently as LIRGs. The cumulative distributions of $M_{\text{H}_2,\text{CO}}$ and $M_{\text{H}_2,\text{CO}}/M_*$ for LIRGs resemble more closely those for QSO2s while showing statistical differences to those for QSO1s.
3. LIRGs and QSO2s show close resemblance in [C II] related quantities: L_{CII} , $L_{\text{CII}}/L_{160\mu\text{m}}$, $L'_{\text{CO}}/L_{\text{CII}}$. QSO1s show larger scatters in these quantities and tend to lie off the relations formed by LIRGs and QSO2s. Comparisons between L_{CII} and SFR derived from total IR luminosity imply that [C II] emission in LIRGs and QSO2s trace SF. The [C II] observations of 5 nearby QSO1s presented here provide tantalizing hints that [C II] emission in QSO1s may have multiple origins, although more data are needed to corroborate this possibility. L'_{CO} in all three samples follows a tight correlation with SFR_{IR} .
4. While [C II] emission could be enhanced by AGN and shocks, we do not observe this enhancement in our samples of QSO2s and LIRGs with high AGN fractions. The extra [C II] emission observed in QSO1s may have significant contributions from other ISM components that are more diffuse and warm, in neutral or ionized phases. The difference in observed L_{CII} hints at different interstellar radiation fields, indicating dissimilar ISM spatial distributions between QSO1s and QSO2s. Tighter constraints on the origins of the [C II] emission in QSOs require a larger sample than what is available in this study as well as new FIR observational facilities.
5. The evolutionary scenario where LIRGs evolve into QSO2s and then to QSO1s predicts a decrease in gas fraction along the sequence. The CO and [C II] data we present here suggest that this scenario might not hold in the nearby universe. Nearby QSO2s could emerge from LIRGs based on their similar gas content, but they are unlikely the precursors of nearby QSO1s. The differences in ISM between QSO1s and QSO2s suggested by the CO and [C II] data presented in this work also disagree with the simple orientation-based unified model. Future data of spatially resolved observations at different redshifts are required to further investigate the evolution of QSOs through cosmic time.

Fig. Set 1. IRAM CO spectra with SDSS cutouts*Facilities:* IRAM, SOFIA(FIFI-LS)*Software:* astropy (Astropy Collaboration et al. 2018), lifelines (Davidson-Pilon 2019), SOSPEX (Fadda & Chambers 2018)

1 YL, AP, and DF gratefully acknowledge the support of
 2 grant SOF-08-0226 from USRA. YL acknowledges support
 3 from the Space Telescope Science Institute Director’s Dis-
 4 cretionary Research Fund grant D0101.90281. RJ was in
 5 part supported by an appointment to the NASA Postdoc-
 6 toral Program at the NASA Jet Propulsion Laboratory, ad-
 7 ministered by Universities Space Research Association un-
 8 der contract with NASA. A. M. J. gratefully acknowledge
 9 the support of grant SOF-08-0038 from USRA and the Max
 10 Planck Society. This work is based on observations made
 11 with the NASA/ DLR Stratospheric Observatory for Infrared
 12 Astronomy (SOFIA). SOFIA is jointly operated by the Uni-
 13 versities Space Research Association, Inc. (USRA), under
 14 NASA contract NNA17BF53C, and the Deutsches SOFIA
 15 Institut (DSI) under DLR contract 50 OK 0901 to the Uni-
 16 versity of Stuttgart. The Herschel spacecraft was designed,
 17 built, tested, and launched under a contract to ESA managed
 18 by the Herschel/Planck Project team by an industrial con-
 19 sortium under the overall responsibility of the prime con-
 20 tractor Thales Alenia Space (Cannes), and including As-
 21 trium (Friedrichshafen) responsible for the payload module
 22 and for system testing at spacecraft level, Thales Alenia
 23 Space (Turin) responsible for the service module, and As-
 24 trium (Toulouse) responsible for the telescope, with in excess
 25 of a hundred subcontractors.

6. ADDITIONAL INFORMATION

Here we provide tables that summarize the ancillary data
 for our IRAM QSO2 sample as well as for the LIRGs
 (GOALS) and QSO1s (PG QSO) comparison samples. These
 data include the CO, [C II], M_* , and FIR data we obtain from
 the literature and some derived properties such as CO lumi-
 nosity in L_{\odot} unit.

Table 1. Summary of CO (1–0) observations for QSO2s with the IRAM 30m telescope.

Source	R.A.	Dec.	z	t_{obs}^a	$\sigma(T_A^*)^b$	$\nu_{\text{CO}(1-0)}^c$	V_{offset}^d	FWHM	$I_{\text{CO}(1-0)}^e$	$L'_{\text{CO}(1-0)}^f$	R_{21}
(1)	(2)	(3)	(4)	(5)	(6)	(7)	(8)	(9)	(10)	(11)	(12)
	°	°		hr	μK	GHz	km/s	km/s	K km/s	10^8 K km/s pc^2	
SDSS01	220.159	53.504	0.0370	2.0	714	111.158	188 ± 39	370 ± 100	1.008 ± 0.216	4.1 ± 0.9	
SDSS02	158.536	60.031	0.0511	2.1	788	109.667	-91 ± 43	387 ± 89	0.790 ± 0.247	6.0 ± 1.9	
SDSS03	163.034	6.154	0.0522	2.5	700	109.552	-3 ± 31	304 ± 60	0.674 ± 0.188	5.4 ± 1.5	
SDSS04	130.937	35.828	0.0539	1.6	602	109.376	17 ± 23	342 ± 40	1.232 ± 0.174	10.4 ± 1.5	0.80
SDSS05	119.921	50.840	0.0544	1.2	737	109.324	-17 ± 16	176 ± 30	0.736 ± 0.142	6.3 ± 1.2	
SDSS06	194.712	52.654	0.0552	1.4	522	109.241	56 ± 51	379 ± 86	0.441 ± 0.161	3.9 ± 1.4	
SDSS07	178.360	58.112	0.0645	3.5	425	108.287	77 ± 18	187 ± 31	0.362 ± 0.085	4.3 ± 1.0	1.35
SDSS08	120.906	39.443	0.0656	2.3	542	108.175			< 0.488	< 6.0	
SDSS09	178.190	10.273	0.0699	2.5	401	107.740			< 0.358	< 5.0	
SDSS10	200.942	61.067	0.0713	1.9	457	107.599			< 0.409	< 5.9	
SDSS11	238.107	27.895	0.0745	0.0		107.279					
SDSS12	124.676	36.069	0.0758	1.0	668	107.149			< 0.598	< 9.7	
SDSS13	120.578	30.773	0.0766	1.5	523	107.069			< 0.468	< 7.7	
SDSS14	165.554	64.990	0.0776	0.7	680	106.970	70 ± 25	334 ± 42	1.187 ± 0.195	20.1 ± 3.3	0.45
SDSS15	211.422	40.442	0.0806	1.0	810	106.673			< 0.727	< 13.2	
SDSS16	120.721	25.882	0.0811	0.0		106.624					
SDSS17	189.681	9.460	0.0829	2.5	473	106.447			< 0.425	< 8.2	
SDSS18	136.975	52.191	0.0848	0.5	1245	106.260			< 1.119	< 22.4	
SDSS19	217.625	13.653	0.0851	2.4	292	106.231	57 ± 44	536 ± 123	0.599 ± 0.115	12.1 ± 2.3	0.85
SDSS20	30.599	12.788	0.0859	1.2	779	106.153	-23 ± 74	556 ± 101	1.200 ± 0.314	24.6 ± 6.4	

NOTE—The columns are: (1) Source name (2) R.A. (3) Dec. (4) Redshift (5) On-source observation time (6) RMS baseline fluctuations (7) Expected line frequency (8) Offset with respect to the expected frequency of the best fit Gaussian (9) Best fit Gaussian line width (FWHM) (10) CO intensity (11) CO luminosity (12) $\frac{L'_{\text{CO}(2-1)}}{L'_{\text{CO}(1-0)}}$ if both lines are robustly detected.

^aEffective integration time is $2t_{\text{obs}}$ by combining both polarizations.

^bUsing 64 resolution elements of 25 MHz.

^cBased on optical redshift.

^dRelative to optical redshift.

^eIn units of T_A^* .

^fIn units of T_{mb} .

Table 2. Summary of CO (2–1) observations for QSO2s with the IRAM 30m telescope.

Source	R.A.	Dec.	z	t_{obs}^a	$\sigma(T_A^*)^b$	$\nu_{\text{CO}(2-1)}^c$	V_{offset}^d	FWHM	$I_{\text{CO}(2-1)}^e$	$L'_{\text{CO}(2-1)}^f$	R_{21}
	°	°		hr	μK	GHz	km/s	km/s	K km/s	10^8 K km/s pc^2	
(1)	(2)	(3)	(4)	(5)	(6)	(7)	(8)	(9)	(10)	(11)	(12)
SDSS01	220.159	53.504	0.0370	0.3	4794	222.312			< 2.594	< 4.2	
SDSS02	158.536	60.031	0.0511	1.2	2367	219.330			< 1.287	< 3.9	
SDSS03	163.034	6.154	0.0522	0.7	5630	219.101			< 3.061	< 9.6	
SDSS04	130.937	35.828	0.0539	1.6	2372	218.748	35 ± 39	240 ± 67	2.501 ± 0.428	8.3 ± 1.4	0.80
SDSS05	119.921	50.840	0.0544	0.0		218.644					
SDSS06	194.712	52.654	0.0552	1.4	904	218.478			< 0.492	< 1.7	
SDSS07	178.360	58.112	0.0645	2.1	586	216.569	70 ± 14	244 ± 27	1.226 ± 0.107	5.8 ± 0.5	1.35
SDSS08	120.906	39.443	0.0656	1.1	1170	216.346			< 0.651	< 3.2	
SDSS09	178.190	10.273	0.0699	0.6	923	215.476			< 0.504	< 2.8	
SDSS10	200.942	61.067	0.0713	2.0	570	215.195			< 0.312	< 1.8	
SDSS11	238.107	27.895	0.0745	1.0	1396	214.554			< 0.775	< 4.8	
SDSS12	124.676	36.069	0.0758	0.0		214.294					
SDSS13	120.578	30.773	0.0766	0.0		214.135					
SDSS14	165.554	64.990	0.0776	1.0	838	213.937	67 ± 13	243 ± 22	1.352 ± 0.154	9.0 ± 1.0	0.45
SDSS15	211.422	40.442	0.0806	1.8	989	213.343	57 ± 18	126 ± 38	0.409 ± 0.119	2.9 ± 0.9	
SDSS16	120.721	25.882	0.0811	1.5	1252	213.244	11 ± 37	220 ± 54	0.403 ± 0.215	2.9 ± 1.6	
SDSS17	189.681	9.460	0.0829	0.0		212.889					
SDSS18	136.975	52.191	0.0848	1.6	1195	212.517			< 0.656	< 5.2	
SDSS19	217.625	13.653	0.0851	1.4	1352	212.458	160 ± 35	330 ± 63	1.292 ± 0.308	10.3 ± 2.4	0.85
SDSS20	30.599	12.788	0.0859	0.0		212.301					

NOTE—The columns are: (1) Source name (2) R.A. (3) Dec. (4) Redshift (5) On-source observation time (6) RMS baseline fluctuations (7) Expected line frequency (8) Offset with respect to the expected frequency of the best fit Gaussian (9) Best fit Gaussian line width (FWHM) (10) CO intensity (11) CO luminosity (12) $\frac{L'_{\text{CO}(2-1)}}{L'_{\text{CO}(1-0)}}$ if both lines are robustly detected.

^aEffective integration time is $2t_{\text{obs}}$ by combining both polarizations.

^bUsing 64 resolution elements of 25 MHz.

^cBased on optical redshift.

^dRelative to optical redshift.

^eIn units of T_A^* .

^fIn units of T_{mb} .

Table 3. Summary of [C II] observations with SOFIA FIFI-LS.

Source	Type	R.A. ◦	Dec. ◦	z	$I_{[\text{OIII}]88\mu\text{m}}$ $\times 10^{-17} \text{ W/m}^2$	$I_{[\text{CII}]158\mu\text{m}}$ $\times 10^{-17} \text{ W/m}^2$	$I_{[\text{CII}]158\mu\text{m,ext}}$ $\times 10^{-17} \text{ W/m}^2$
(1)	(2)	(3)	(4)	(5)	(6)	(7)	(8)
Mrk 290 (PG 1534+580)	QSO1	233.970	57.902	0.0296	2.9	<1.6	
UGC 05025 (PG 0923+129)	QSO1	141.514	12.734	0.0288	9.5	7.2	18
Mrk 110 (PG 0921+525)	QSO1	141.304	52.286	0.0353		7.0	15
IISZ010 (PG 1310-108)	QSO1	198.274	-11.128	0.0343		3.9	
Mrk335 (PG 0003+199)	QSO1	1.581	20.203	0.0258	5.2	6.0	20
SDSS01	QSO2	220.159	53.504	0.0370		5.7	10
SDSS02	QSO2	158.536	60.031	0.0511	7.5	4.0	8.7
SDSS03	QSO2	163.034	6.154	0.0522		1.9	
SDSS04	QSO2	130.937	35.828	0.0539		2.5	
SDSS07	QSO2	178.360	58.112	0.0645		0.8	1.4

NOTE—The columns are: (1) Source name (2) Source type (3) R.A. (4) Dec. (5) Redshift (6) [O III] 88 μm line intensity within the PSF aperture (diameter 8.8'') (7) [C II] 158 μm line intensity within the PSF aperture (diameter 15.2'') (8) [C II] 158 μm line intensity within an extended aperture (diameter 30'' for UGC 05025, diameter 22'' for others to best capture all extended flux). The uncertainty in the measured line intensities is dominated by the calibration error (15%, except for IISZ010 which has a 25% error due to higher background uncertainty).

Table 4. Two-sample statistical test results on L'_{CO} , $L_{160\mu\text{m}}$, $L'_{\text{CO}}/L_{160\mu\text{m}}$, M_* , $M_{\text{H}_2,\text{CO}}$, and $M_{\text{H}_2,\text{CO}}/M_*$ of QSO1s, QSO2s, and LIRGs

Comparison pair	Test statistics	Test p-values
	$t_{\text{logrank}}, t_{\text{peto}}, t_{\text{wilcoxon}}, t_{\text{tarone}}^a$	$p_{\text{logrank}}, p_{\text{peto}}, p_{\text{wilcoxon}}, p_{\text{tarone}}^b$
LIRGs (63), QSO1s (40)^c		
$\log(L'_{\text{CO}})$	36.4, 26.1, 25.1, 30.8	$1.6 \times 10^{-9}, 3.3 \times 10^{-7}, 5.3 \times 10^{-7}, 2.9 \times 10^{-8}$
$\log(L_{160\mu\text{m}})$	34.6, 29.8, 29.1, 32.8	$4.1 \times 10^{-9}, 4.8 \times 10^{-8}, 7.0 \times 10^{-8}, 1.0 \times 10^{-8}$
$L'_{\text{CO}}/L_{160\mu\text{m}}$	0.03, 0.4, 0.4, 0.07	0.9, 0.6, 0.5, 0.8
M_*	5.0, 3.4, 3.2, 4.1	0.03, 0.07, 0.07, 0.04
$M_{\text{H}_2,\text{CO}}$	20.0, 11.4, 10.8, 14.9	$7.8 \times 10^{-6}, 7.4 \times 10^{-4}, 1.0 \times 10^{-3}, 1.1 \times 10^{-4}$
$M_{\text{H}_2,\text{CO}}/M_*$	17.0, 8.2, 7.8, 11.6	$3.7 \times 10^{-5}, 4.1 \times 10^{-3}, 5.3 \times 10^{-3}, 6.5 \times 10^{-4}$
LIRGs (63), QSO2s (20)		
$\log(L'_{\text{CO}})$	30.7, 24.6, 23.9, 27.9	$3.1 \times 10^{-8}, 6.9 \times 10^{-7}, 1.0 \times 10^{-6}, 1.3 \times 10^{-7}$
$\log(L_{160\mu\text{m}})$	16.7, 24.9, 24.9, 24.0	$4.3 \times 10^{-5}, 6.0 \times 10^{-7}, 6.0 \times 10^{-7}, 9.9 \times 10^{-7}$
$L'_{\text{CO}}/L_{160\mu\text{m}}$	0.20, 0.06, 0.04, 0.10	0.7, 0.8, 0.8, 0.8
M_*	3.7, 7.0, 7.0, 6.0	0.05, 0.01, 0.01, 0.01
$M_{\text{H}_2,\text{CO}}$	4.5, 6.4, 6.3, 6.3	0.03, 0.01, 0.01, 0.01
$M_{\text{H}_2,\text{CO}}/M_*$	0.63, 0.18, 0.14, 0.32	0.43, 0.67, 0.71, 0.57
QSO1s (40), QSO2s (20)		
$\log(L'_{\text{CO}})$	0.16, 0.15, 0.45, 0.05	0.7, 0.7, 0.5, 0.8
$\log(L_{160\mu\text{m}})$	2.2, 0.17, 0.07, 0.65	0.1, 0.7, 0.8, 0.4
$L'_{\text{CO}}/L_{160\mu\text{m}}$	0.002, 0.2, 0.3, 0.1	1.0, 0.7, 0.6, 0.8
M_*	0.002, 0.8, 0.9, 0.3	1.0, 0.4, 0.4, 0.6
$M_{\text{H}_2,\text{CO}}$	1.3, 0.18, 0.02, 0.3	0.3, 0.7, 0.9, 0.6
$M_{\text{H}_2,\text{CO}}/M_*$	2.3, 1.5, 1.4, 1.7	0.13, 0.22, 0.24, 0.19

^aThe calculated test statistics from the Logrank, Peto-Peto, Wilcoxon and Tarone–Ware two-sample tests.

^bThe derived p -values from the Logrank, Peto-Peto, Wilcoxon and Tarone–Ware two-sample tests.

^cThe sizes of the samples that go into the tests. For $L'_{\text{CO}}/L_{160\mu\text{m}}$, we do not include in tests the two QSO1s for which both L'_{CO} and $L_{160\mu\text{m}}$ are upper limits.

Table 5. LIRGs literature data.

Name	z	M_*	$L_{160\mu\text{m}}$	$\Delta L_{160\mu\text{m}}$	FAGN	$I_{\text{[CII]}}$	$\Delta I_{\text{[CII]}}$	$L_{\text{[CII]}}$	$\Delta L_{\text{[CII]}}$	CO ref	L'_{CO}	$\Delta L'_{\text{CO}}$	L_{CO}	ΔL_{CO}	$M_{\text{H}_2, \text{CO}}$	SFR _{IR}	$\Delta \text{SFR}_{\text{IR}}$
(1)	(2)	(3)	(4)	(5)	(6)	(7)	(8)	(9)	(10)	(11)	(12)	(13)	(14)	(15)	(16)	(17)	(18)
		$\log(M_\odot)$	$\log(L_\odot)$	$\log(L_\odot)$		$\times 10^{-17} \text{ Wm}^2$	$\times 10^{-17} \text{ Wm}^2$	$\log(L_\odot)$	$\log(L_\odot)$		$\log(\text{K km/s pc}^2)$	$\log(\text{K km/s pc}^2)$	$\log(L_\odot)$	$\log(L_\odot)$	$\log(M_\odot)$	M_\odot/yr	M_\odot/yr
NGC 0232S	0.02217	11.04	10.86	0.019	0.01	138.0	2.32	8.6	0.007	1	9.66	0.04	5.38	0.04	9.91	21.28	0.835
NGC 0232N	0.02217	10.93	10.14	0.019	0.71	26.06	2.22	7.88	0.037	1	9.29	0.067	5.01	0.067	9.55	4.79	0.189
IC 1623AB	0.02007	11.21	10.98	0.022	0.47	561.57	2.78	9.13	0.002	2	9.93	0.043	5.62	0.002	10.18	26.79	1.213
MCG -03-04-014	0.03349	11.21	11.04	0.019	0.0	143.43	3.11	8.99	0.009	2	9.73	0.044	5.38	0.005	9.99	30.46	1.215
CGCG 436-030	0.03123	10.85	10.87	0.019	0.35	121.38	1.62	8.85	0.006	1	9.5	0.026	5.24	0.026	9.76	21.35	0.851
IRAS F01364-1042	0.04825	10.64	11.01	0.019	0.12	14.25	0.62	8.31	0.019	2	9.6	0.046	5.29	0.016	9.86	28.59	1.122
NGC 0695	0.03247	11.3	11.12	0.022	0.0	283.75	1.35	9.26	0.002	1	10.01	0.013	5.75	0.013	10.26	36.12	1.626
UGC 01385	0.01875	10.68	10.33	0.019	0.0	60.28	0.54	8.1	0.004	1	9.01	0.012	4.74	0.012	9.27	7.06	0.285
UGC 02238	0.02188	10.94	10.85	0.022	0.0	266.56	1.92	8.88	0.003	1	9.41	0.008	5.14	0.008	9.66	20.78	0.929
NGC 1275	0.01756	11.63	10.28	0.022	0.97	162.31	3.73	8.47	0.01	1	9.11	0.02	4.83	0.02	9.36	6.37	0.288
IRAS F03359+1523	0.03354	10.75	10.83	0.019	0.0	47.38	2.02	8.56	0.019	1	9.55	0.061	5.29	0.061	9.8	19.68	0.773
CGCG 465-012N	0.02222	10.67	10.34	0.022	0.0	108.49	1.47	8.5	0.006	1	9.15	0.016	4.88	0.016	9.4	7.24	0.326
CGCG 465-012S	0.02222	10.84	10.58	0.022	0.0	138.49	1.44	8.61	0.006	1	9.48	0.008	5.21	0.008	9.74	11.71	0.528
CGCG 468-002S	0.01819	10.82	9.93	0.016	0.79	18.88	0.6	7.57	0.014	1	8.93	-5.088	4.64	-0.715	9.18	3.1	0.102
CGCG 468-002N	0.01819	10.26	10.37	0.017	0.0	54.22	0.65	8.02	0.005	1	8.92	-5.131	4.64	-0.721	9.18	7.58	0.265
IRAS 05083+2441	0.02307	10.75	10.44	0.019	0.0	127.98	1.35	8.61	0.005	1	8.89	0.062	4.61	0.062	9.15	8.81	0.34
IRAS 05129+5128	0.02743	10.71	10.62	0.019	0.01	108.86	0.93	8.69	0.004	1	9.39	0.04	5.11	0.04	9.65	12.73	0.499
IRAS F05189-2524	0.04256	11.5	11.08	0.019	0.94	23.53	2.6	8.42	0.048	2	9.42	0.044	5.1	0.047	9.67	33.57	1.315
UGC 03410S	0.01308	10.93	10.54	0.022	0.0	388.21	2.35	8.59	0.003	1	9.05	0.047	4.71	0.047	9.3	10.89	0.492
UGC 03410N	0.01308	10.57	10.92	0.022	0.0	101.92	1.0	8.01	0.004	1	9.35	0.038	5.0	0.038	9.6	3.41	0.154
NGC 2342	0.0176	11.1	10.66	0.022	0.0	322.59	1.65	8.77	0.002	2	9.19	0.044	4.88	0.007	9.45	13.96	0.626
NGC 2341	0.0176	10.85	10.48	0.022	...	254.15	1.5	8.67	0.003	2	9.14	0.044	4.86	0.01	9.4	9.51	0.428
NGC 2623	0.01851	10.81	10.82	0.019	0.13	68.72	1.87	8.14	0.012	1	9.2	0.032	4.86	0.032	9.45	19.29	0.767
UGC 05101	0.03937	11.29	11.43	0.018	0.71	71.25	3.91	8.83	0.024	2	9.79	0.044	5.48	0.008	10.04	68.94	2.638
MCG +08-18-01EN	0.02594	10.83	10.68	0.019	...	67.88	1.52	8.44	0.01	1	9.23	0.031	4.92	0.031	9.49	14.42	0.57
IRAS F10173+0828	0.04909	10.56	10.92	0.019	0.19	3.61	1.18	7.73	0.142	1	9.64	0.044	5.35	0.044	9.89	23.89	0.956
CGCG 011-076	0.0249	11.12	10.73	0.019	0.25	85.87	2.0	8.5	0.01	2	9.5	0.045	5.2	0.01	9.76	16.24	0.647
IC 2810W	0.034	11.08	10.91	0.019	0.0	44.12	1.56	8.49	0.015	1	9.33	0.054	5.0	0.054	9.58	23.2	0.892
IC 2810E	0.034	10.8	10.6	0.018	...	19.62	0.61	8.14	0.014	1	9.36	0.042	5.03	0.042	9.61	12.34	0.466
ESO 507-G070	0.0217	11.09	10.74	0.019	0.0	96.86	2.69	8.43	0.012	2	9.42	0.045	5.12	0.012	9.67	16.35	0.649
UGC 08387	0.0233	10.83	11.03	0.019	0.0	172.03	2.01	8.74	0.005	1	9.73	0.015	5.37	0.015	9.99	30.05	1.212
NGC 5104	0.01861	11.13	10.66	0.019	0.08	128.49	1.69	8.42	0.006	2	9.31	0.044	5.01	0.01	9.57	13.95	0.554
IC 4280	0.01631	11.16	10.56	0.022	0.0	263.55	1.11	8.62	0.002	2	9.16	0.045	4.85	0.013	9.41	11.42	0.517
UGC 08739	0.01679	11.0	10.69	0.022	0.05	234.15	1.76	8.57	0.003	2	9.43	0.044	5.12	0.006	9.68	14.95	0.67
CGCG 247-020	0.02574	10.74	10.55	0.022	0.0	34.27	0.65	8.13	0.008	2	9.29	0.045	4.97	0.013	9.54	11.09	0.501
IRAS F14348-1447	0.08273	11.57	11.63	0.019	0.57	32.8	1.32	9.16	0.017	2	10.23	0.049	5.92	0.023	10.48	103.14	4.052
CGCG 049-057	0.013	10.29	10.6	0.02	0.02	44.94	1.86	7.65	0.018	2	8.96	0.043	4.65	0.004	9.22	12.36	0.505
NGC 5936	0.01336	10.99	10.47	0.022	0.0	304.26	1.34	8.5	0.002	2	9.1	0.044	4.79	0.005	9.35	9.32	0.42
Arp 220	0.01813	11.06	11.49	0.02	0.67	137.44	6.1	8.43	0.019	1	9.57	0.022	5.18	0.022	9.82	78.07	3.248
IRAS F16164-0746	0.02715	10.87	10.92	0.019	0.0	79.94	0.94	8.55	0.005	2	9.43	0.046	5.24	0.013	9.68	23.69	0.94
CGCG 052-037	0.02449	11.07	10.81	0.019	0.0	114.93	1.95	8.61	0.007	2	9.44	0.044	5.13	0.006	9.69	21.14	0.762
NGC 6286	0.01835	11.1	10.87	0.022	0.0	296.82	1.32	8.77	0.002	2	9.63	0.044	5.31	0.005	9.89	19.13	0.964
NGC 6285	0.01835	10.58	10.05	0.019	...	68.33	1.88	8.13	0.012	2	9.04	0.045	4.69	0.013	9.29	3.91	0.154
IRAS F17207-0014	0.04281	11.18	11.67	0.019	0.14	100.4	2.97	9.05	0.013	1	9.6	-1.083	5.29	-0.915	9.85	112.05	4.459

Table 5 continued

Table 5 (continued)

Name	z	M*	$L_{160\mu\text{m}}$	$\Delta L_{160\mu\text{m}}$	FAGN	$I_{\text{[CII]}}$	$\Delta I_{\text{[CII]}}$	$L_{\text{[CII]}}$	$\Delta L_{\text{[CII]}}$	COref	L'_{CO}	$\Delta L'_{\text{CO}}$	L_{CO}	ΔL_{CO}	$M_{\text{H}_2, \text{CO}}$	SFRIR	ΔSFRIR
(1)	(2)	(3)	(4)	(5)	(6)	(7)	(8)	(9)	(10)	(11)	(12)	(13)	(14)	(15)	(16)	(17)	(18)
		$\log(M_{\odot})$	$\log(L_{\odot})$	$\log(L_{\odot})$		$\times 10^{-17} \text{ Wm}^{-2}$	$\times 10^{-17} \text{ Wm}^{-2}$	$\log(L_{\odot})$	$\log(L_{\odot})$		$\log(\text{K km/s pc}^{-2})$	$\log(\text{K km/s pc}^{-2})$	$\log(L_{\odot})$	$\log(L_{\odot})$	$\log(M_{\odot})$	M_{\odot}/yr	M_{\odot}/yr
UGC 11041	0.01628	10.9	10.5	0.022	0.0	226.91	1.65	8.55	0.003	2	9.29	0.044	4.98	0.006	9.54	10.09	0.456
CGCG 141-034	0.01983	10.75	10.53	0.019	0.09	67.24	2.45	8.19	0.016	2	8.99	0.048	4.67	0.021	9.25	10.61	0.416
ESO 593-IG008	0.04873	11.55	11.36	0.019	0.0	135.7	3.24	9.32	0.01	2	10.09	0.045	5.78	0.001	10.35	59.86	2.381
NGC 6907	0.01064	11.19	10.59	0.022	0.0	314.32	1.55	8.32	0.002	2	9.15	0.044	4.84	0.007	12.14	18.94	0.754
ESO 602-G025	0.02504	11.14	10.81	0.019	0.16	135.48	2.4	8.7	0.008	2	9.59	0.044	5.27	0.006	9.84	18.34	0.724
UGC 12150	0.02139	11.04	10.79	0.019	0.01	95.97	2.96	8.42	0.013	2	9.21	0.046	4.9	0.015	9.47	18.34	0.724
IRAS F22491-1808	0.07776	11.36	11.25	0.019	0.11	17.09	0.43	8.82	0.011	2	9.74	0.045	5.43	0.013	10.0	47.71	1.835
CGCG 453-062	0.0251	10.95	10.81	0.019	0.0	106.99	2.43	8.6	0.01	2	9.23	0.049	4.93	0.022	9.49	18.92	0.754
IC 5298	0.02742	11.11	10.82	0.019	0.75	59.06	1.2	8.42	0.009	1	9.31	0.032	5.03	0.032	9.56	19.54	0.778
NGC 771S1	0.01427	11.37	10.91	0.022	0.0	315.9	2.63	8.88	0.004	1	9.45	0.011	5.16	0.011	9.71	23.54	1.057
Mrk 331	0.01848	10.92	10.8	0.019	0.0	207.63	1.37	8.62	0.003	1	8.82	0.085	4.53	0.085	9.07	18.71	0.742
MCG +12-02-001	0.0157	10.91	10.74	0.022	0.0	0.434	1	8.93	0.028	4.62	0.028	9.19
MCG +08-18-013S	0.02594	9.8	9.39	0.026	0.434	1	9.24	-2.485	4.92	-0.768	9.49
CGCG 011-076F	0.0249	9.98	9.47	0.021	0.434	1	9.01	0.059	4.66	0.058	9.27
NGC 771S2	0.01427	10.41	9.88	0.022	0.28	0.434	1	8.61	0.039	4.32	0.039	8.86
NGC 0034	0.01962	11.04	10.65	0.02	0.17	0.434	2	9.33	0.045	5.03	0.012	9.59
NGC 0958	0.01914	11.45	10.91	0.022	0.434	2	9.39	0.045	5.07	0.013	9.64
ESO 550-IG025	0.03209	11.06	10.91	0.022	0.434	2	9.52	0.047	5.21	0.017	9.78
CGCG 043-099	0.03748	11.08	11.02	0.019	0.0	0.434	2	9.67	0.044	5.36	0.008	9.92
ESO350-IG038	0.0206	10.67	10.03	0.019	0.75	70.56	0.79	8.25	0.005
NGC0877b	0.01305	10.39	9.95	0.022	0.18	76.74	1.89	7.88	0.011
NGC0877a	0.01305	11.14	10.7	0.022	0.31	290.92	1.66	8.46	0.002
MCG+06-36b	0.03371	11.28	10.6	0.018	0.0	38.14	1.84	8.42	0.021
MCG+05-06-36a	0.03371	10.99	11.01	0.019	0.12	71.72	2.09	8.69	0.013
NGC1068	0.00379	11.16	10.65	0.022	...	2489.28	6.25	8.31	0.001
UGC02982	0.0177	10.93	10.73	0.022	0.0	424.92	1.87	8.89	0.002
ESO203-IG001	0.05291	10.87	10.95	0.018	0.9	8.87	2.19	8.19	0.107
MCG-05-12-006	0.01875	10.64	10.42	0.019	0.0	44.46	1.57	7.96	0.015
NGC1961	0.01312	11.59	10.81	0.022	0.46	196.93	2.97	8.3	0.007
NGC2146	0.00298	10.81	10.22	0.022	0.0	3130.97	10.07	8.2	0.001
NGC2369	0.01081	11.09	10.68	0.022	0.08	344.82	1.7	8.37	0.002
NGC2388a	0.01379	10.89	10.64	0.02	...	214.53	1.86	8.38	0.004
NGC2388b	0.01379	10.58	10.14	0.022	...	155.23	1.97	8.24	0.006
MCG+02-20-003	0.01625	10.69	10.46	0.019	0.7	117.11	1.35	8.26	0.005
ESO60-IG016	0.04632	10.97	10.92	0.022	...	53.63	1.52	8.85	0.012
IRASF08572+3915	0.05835	11.8	10.86	0.018	...	12.6	1.36	8.43	0.047
IRAS09022-3615	0.05964	11.22	11.5	0.019	0.73	93.49	1.68	9.32	0.008
NGC3110a	0.01686	11.12	10.77	0.022	0.0	451.52	2.49	8.88	0.002
IC2545	0.0341	11.46	10.81	0.019	0.95	45.03	1.1	8.5	0.011
NGC3236	0.00935	11.06	10.95	0.022	0.0	1537.24	2.26	8.89	0.001
ESO564-G036	0.02101	11.39	10.81	0.022	0.12	188.1	1.28	8.69	0.003
IRASF10565+2448	0.0431	11.17	11.33	0.019	0.06	78.13	2.48	8.95	0.014
ESO320-G030	0.01078	10.67	10.64	0.02	0.0	257.94	1.94	8.24	0.003
IRASF12112+0305	0.07332	11.34	11.54	0.019	0.21	36.63	3.07	9.1	0.026
ESO367-G030b	0.01849	10.98	10.43	0.022	0.0	128.03	1.6	8.41	0.005
ESO367-G030a	0.01849	11.21	10.54	0.022	0.09	208.38	1.82	8.62	0.004
VV250b	0.03107	10.66	10.37	0.016	0.0	36.5	1.04	8.33	0.012

Table 5 continued

Table 5 (continued)

Name	z	M*	$L_{160\mu\text{m}}$	$\Delta L_{160\mu\text{m}}$	FAGN	$L_{\text{[CII]}}$	$\Delta L_{\text{[CII]}}$	$L_{\text{[CII]}}$	$\Delta L_{\text{[CII]}}$	COref	L'_{CO}	$\Delta L'_{\text{CO}}$	L_{CO}	ΔL_{CO}	$M_{\text{H}_2, \text{CO}}$	SFRIR	ΔSFRIR
(1)	(2)	(3)	(4)	(5)	(6)	(7)	(8)	(9)	(10)	(11)	(12)	(13)	(14)	(15)	(16)	(17)	(18)
		$\log(M_{\odot})$	$\log(L_{\odot})$	$\log(L_{\odot})$		$\times 10^{-17} \text{ Wm}^{-2}$	$\times 10^{-17} \text{ Wm}^{-2}$	$\log(L_{\odot})$	$\log(L_{\odot})$		$\log(\text{K km s}^{-2})$	$\log(\text{K km s}^{-2})$	$\log(L_{\odot})$	$\log(L_{\odot})$	$\log(M_{\odot})$	M_{\odot}/yr	M_{\odot}/yr
VV250a	0.03107	10.82	10.76	0.018	0.0	80.6	0.67	8.67	0.004
MCG-03-34-064	0.01654	11.08	10.0	0.019	0.98	21.1	1.45	7.53	0.03
NGC5135	0.01369	11.1	10.74	0.022	0.14	225.47	1.54	8.39	0.003
NGC5256	0.02782	11.22	10.78	0.022	0.0	150.17	2.21	8.84	0.006
NGC5653	0.01188	11.01	10.51	0.02	0.0	414.99	1.66	8.53	0.002
NGC5734a	0.01375	11.09	10.54	0.022	0.12	302.18	2.05	8.52	0.003
NGC5734b	0.01375	10.82	10.28	0.022	0.07	247.23	1.92	8.44	0.003
VV340b	0.03367	10.84	10.4	0.022	0.0	62.81	1.52	8.63	0.011
VV340a	0.03367	11.39	11.15	0.022	0.0	169.55	3.38	9.06	0.009
IRASF15250+3609	0.05516	10.78	11.0	0.019	0.93	14.65	1.49	8.44	0.044
NGC5990	0.01281	11.15	10.41	0.022	0.72	264.1	1.81	8.4	0.003
NGC6052	0.01581	10.68	10.35	0.022	0.0	236.78	0.92	8.54	0.002
NGC6090	0.02984	11.55	10.84	0.019	...	143.31	1.61	8.88	0.005
NGC6240	0.02448	11.59	11.09	0.019	0.34	487.24	5.8	9.24	0.005
IRASF17132+5313	0.05904	11.24	11.21	0.019	0.05	65.58	2.93	9.02	0.019
IC4687c	0.01735	10.7	10.27	0.019	...	107.1	1.59	8.28	0.006
NGC6670Aa	0.0286	10.81	10.44	0.022	0.0	77.78	0.7	8.58	0.004
IC4734	0.01561	10.96	10.74	0.019	0.06	160.72	1.85	8.36	0.005
ESO339-G011	0.0192	11.01	10.6	0.019	0.48	172.52	1.73	8.57	0.004
NGC6926a	0.01961	11.29	10.85	0.022	0.43	200.09	1.55	8.66	0.003
ESO286-IG019	0.043	11.05	11.06	0.019	0.77	57.93	1.04	8.82	0.008
ESO286-G035	0.01736	10.77	10.54	0.02	0.0	185.68	1.84	8.52	0.004
NGC7130	0.01615	11.16	10.75	0.022	0.41	237.74	0.95	8.56	0.002
IC5179	0.01141	11.09	10.69	0.022	0.0	722.85	1.39	8.74	0.001
NGC7469	0.01632	11.29	10.87	0.019	0.58	286.81	1.7	8.65	0.003
ESO148-IG002	0.0446	11.03	11.11	0.019	0.4	94.85	1.85	9.06	0.008
NGC7552	0.00536	10.88	10.44	0.022	0.02	729.03	2.04	8.08	0.001
ESO077-IG014a	0.04156	11.09	11.13	0.022	0.1	18.7	0.58	8.29	0.013
IRASF23365+3604	0.06448	11.15	11.38	0.019	0.22	20.34	1.92	8.73	0.041
MCG-01-60-022	0.02324	10.85	10.61	0.019	0.0	160.18	1.61	8.71	0.004

NOTE.—The columns are: (1) Galaxy name; (2) Redshift from Chu et al. (2017); (3) Stellar mass from Howell et al. (2010) (4K5) Luminosity and its uncertainty at $160\mu\text{m}$ derived from fluxes in Chu et al. (2017) as described in §4.1; (6) The fractional contribution of AGN to MIR luminosity (AGN fractions) calculated following the method in Pérez et al. (2011) (7)(8) Galaxy-integrated flux and uncertainty of the [C II] line measured from the best aperture in Diaz-Santos et al. (2017) (9)(10) Columns (7)(8) converted to luminosity in solar unit (11) The reference for the CO luminosity (12)(13) CO luminosity and its uncertainty in brightness temperature unit (14)(15) Columns (12)(13) converted to solar unit; (16) The H_2 mass derived in §4.1.1 using $\alpha_{\text{CO}} = 1.8 (\text{K km s}^{-1} \text{pc}^2)^{-1}$ (Herrero-Illana et al. 2019; Montoya Amoyave et al. 2023) (17)(18) Star formation rate and its uncertainty based on the total infrared luminosity derived from the luminosity at $160\mu\text{m}$ as described in §4.1.2.

References—(1) Yamashita et al. (2017), (2) Herrero-Illana et al. (2019)

Table 6. QSOs (PG QSO) literature and derived data.

Name	z	L'_{CO} $\log(\text{K km/s pc}^2)$	$\Delta L'_{\text{CO}}$ $\log(\text{K km/s pc}^2)$	M_* $\log(M_{\odot})$	$L_{160\mu\text{m}}$ $\log(L_{\odot})$	$\Delta L_{160\mu\text{m}}$ $\log(L_{\odot})$	L_{CO} $\log(L_{\odot})$	ΔL_{CO} $\log(L_{\odot})$	CO ref	L_{CII} $\log(L_{\odot})$	ΔL_{CII} $\log(L_{\odot})$	SFR _{IR} M_{\odot}/yr	$\Delta\text{SFR}_{\text{IR}}$ M_{\odot}/yr	$M_{\text{H}_2, \text{CO}}$ $\log(M_{\odot})$
(1)	(2)	(3)	(4)	(5)	(6)	(7)	(8)	(9)	(10)	(11)	(12)	(13)	(14)	(15)
PG 0003+199	0.026	7.23	0.06	10.38	8.9	0.129	3.56	0.055	1	7.9	0.065	0.36	0.097	7.75
PG 0007+106	0.089	8.63	0.05	11.03	10.3	0.095	4.92	0.047	1	9.15
PG 0050+124	0.061	9.71	0.02	11.31	10.9	0.009	5.4	0.016	3	10.23
PG 0934+013	0.05	8.49	0.03	10.1	9.9	0.083	4.79	0.025	1	9.01
PG 1011-040	0.058	9.02	0.04	10.31	9.9	0.101	4.82	0.038	7	9.54
PG 1119+120	0.05	8.47	0.06	10.86	10.0	0.059	4.18	0.064	3	8.99
PG 1126-041	0.062	9.09	0.04	11.04	10.3	0.033	4.92	0.043	7	9.61
PG 1211+143	0.081	7.94	0.03	10.57	9.4	0.117	4.19	0.034	1	8.46
PG 1229+204	0.063	8.66	0.11	11.13	9.9	0.097	4.34	0.109	6	9.18
PG 1310-108	0.034	7.94	0.02	10.73	9.0	0.38	4.21	0.017	1	7.44	0.109	0.45	0.352	8.46
PG 1404+226	0.098	8.95	0.11	9.99	10.0	0.068	4.65	0.109	6	9.47
PG 1426+015	0.086	9.09	0.07	11.24	10.4	0.077	4.79	0.072	6	9.61
PG 1501+106	0.036	7.49	0.04	11.22	9.6	0.151	3.78	0.04	1	8.01
PG 2130+099	0.063	8.82	0.06	11.04	10.3	0.038	4.55	0.056	3	9.34
PG 2214+139	0.066	8.02	0.05	11.17	9.7	0.147	4.3	0.046	1	8.54
PG 0052+251	0.155	9.36	0.0	11.24	10.6	0.111	5.05	0.0	5	9.88
PG 0157+001	0.163	9.85	0.04	11.72	11.6	0.013	5.54	0.039	3	10.37
PG 0804+761	0.1	8.97	0.11	10.83	9.5	0.105	4.66	0.109	6	9.49
PG 0838+770	0.131	9.31	0.07	11.33	10.7	0.069	5.0	0.069	3	9.83
PG 0844+349	0.064	8.45	...	10.88	10.1	0.109	4.14	...	6	8.97
PG 1202+281	0.165	9.5	...	11.05	10.3	0.183	5.19	...	2	10.02
PG 1309+355	0.183	8.99	...	11.41	10.4	0.132	4.68	...	5	9.51
PG 1351+640	0.088	8.98	0.08	10.82	10.4	0.052	4.68	0.08	3	9.5
PG 1402+261	0.164	9.41	0.0	11.05	10.6	0.1	5.11	0.0	5	9.93
PG 1411+442	0.09	8.82	...	11.03	10.0	0.191	4.53	...	6	9.34
PG 1415+451	0.114	9.11	0.06	10.84	10.1	0.242	4.8	0.062	3	9.63
PG 1440+356	0.079	9.26	0.04	11.24	10.6	0.037	4.97	0.039	3	9.78
PG 1545+210	0.264	9.54	...	11.34	11.8	...	5.23	...	5	10.06
PG 1613+658	0.129	9.8	0.03	11.65	11.2	0.025	5.49	0.033	3	10.32
PG 1700+518	0.292	10.19	0.08	11.58	11.5	0.079	5.91	0.078	4	10.71
PG 0049+171	0.064	7.83	...	11.07	9.2	0.186	4.12	...	1	8.35
PG 0923+129	0.029	8.7	0.01	10.38	9.9	0.026	4.99	0.012	1	7.95	0.065	2.88	0.157	9.22
PG 1244+026	0.048	8.42	0.02	9.7	9.4	0.279	4.71	0.018	1	8.94
PG 1341+258	0.087	7.98	0.1	10.85	9.7	0.063	4.27	0.097	1	8.5
PG 1351+236	0.055	9.03	0.02	11.24	10.1	0.047	5.33	0.015	1	9.55

Table 6 continued

Table 6 (continued)

Name	z	L'_{CO} $\log(\text{K km/s pc}^2)$	$\Delta L'_{\text{CO}}$ $\log(\text{K km/s pc}^2)$	M_* $\log(M_{\odot})$	$L_{160\mu\text{m}}$ $\log(L_{\odot})$	$\Delta L_{160\mu\text{m}}$ $\log(L_{\odot})$	L_{CO} $\log(L_{\odot})$	ΔL_{CO} $\log(L_{\odot})$	CO ref	L_{CII} $\log(L_{\odot})$	ΔL_{CII} $\log(L_{\odot})$	SFR _{IR} M_{\odot}/yr	$\Delta\text{SFR}_{\text{IR}}$ M_{\odot}/yr	$M_{\text{H}_2, \text{CO}}$ $\log(M_{\odot})$
(1)	(2)	(3)	(4)	(5)	(6)	(7)	(8)	(9)	(10)	(11)	(12)	(13)	(14)	(15)
PG 1448+273	0.065	8.55	0.02	10.05	9.9	0.067	4.84	0.02	1	9.07
PG 2209+184	0.07	8.74	0.02	11.41	10.0	0.119	5.04	0.019	1	9.26
PG 2304+042	0.042	7.42	...	11.25	8.7	...	3.71	...	1	7.94
PG 1534+580	0.03	8.7	...	10.96	9.3	0.221	4.39	...	8	6.92	...	0.83	0.382	9.19
PG 0921+525	0.0353	8.26	0.07	10.32	9.04	0.174	3.93	0.081	9	8.05	0.065	0.49	0.175	8.75

NOTE—The columns are: (1) PG name (2) Redshift from Petric et al. (2015) (3)(4) CO(1–0) luminosity and its uncertainty in brightness temperature unit (5) Stellar mass from Xie et al. (2021) (6)(7) Luminosity and its uncertainty at $160\mu\text{m}$ from Petric et al. (2015) (8)(9) Columns (3)(4) converted to solar unit (10) The reference for the CO luminosity (11)(12) [C II] $158\mu\text{m}$ luminosity and its uncertainty used in plots. These values are converted from flux measurements listed in Table 3, using the measurements for extended emission when available (13)(14) Star formation rate and its uncertainty based on the total infrared luminosity derived from the luminosity at $160\mu\text{m}$ as described in §4.1.2 (15) The H_2 mass derived in §4.1.1 using $\alpha_{\text{CO}} = 3.1 (\text{K km s}^{-1} \text{pc}^2)^{-1}$ (Shangguan et al. 2020).

^a Unavailable uncertainty means the corresponding quantity is an upper limit.

References—(1)Shangguan et al. (2020) (2)Evans et al. (2001) (3)Evans et al. (2006) (4)Evans et al. (2009) (5)Casoli & Lomard (2001) (6)Scoville et al. (2003) (7)Bertram et al. (2007) (8)Wyłezalek et al. (2022) (9)Salomé et al. (2023)

Table 7. IRAM QSO2 literature and derived data.

Name	M_*	$L_{160\mu\text{m}}$	$\Delta L_{160\mu\text{m}}$	L_{CO}	ΔL_{CO}	M_* ref	$L_{160\mu\text{m}}$ ref	L_{CII}	ΔL_{CII}	SFR_{IR}	$\Delta \text{SFR}_{\text{IR}}$	$M_{\text{H}_2, \text{CO}}$
	$\log(M_\odot)$	$\log(L_\odot)$	$\log(L_\odot)$	$\log(L_\odot)$	$\log(L_\odot)$			$\log(L_\odot)$	$\log(L_\odot)$	M_\odot/yr	M_\odot/yr	$\log(M_\odot)$
(1)	(2)	(3)	(4)	(5)	(6)	(7)	(8)	(9)	(10)	(11)	(12)	(13)
SDSS01	9.87	10.05	0.028	4.29	0.093	1	2	7.94	0.065	3.91	0.218	9.25
SDSS02	10.97	10.34	0.016	4.47	0.136	3	3	8.15	0.065	7.19	0.239	9.41
SDSS03	10.57	9.97	0.043	4.42	0.121	3	3	7.51	0.065	3.36	0.286	9.37
SDSS04	10.92	10.04	0.018	4.71	0.061	3	3	7.65	0.065	3.83	0.143	9.65
SDSS05	10.61	10.15	0.022	4.49	0.084	3	3	9.43
SDSS06	10.78	9.88	0.049	4.28	0.159	3	3	9.22
SDSS07	10.5	10.04	0.039	4.33	0.102	3	3	7.57	0.065	3.83	0.299	9.27
SDSS08	11.03	9.92	0.049	4.48	...	^a	3	9.41
SDSS09	10.67	9.65	0.091	4.4	...	3	3	9.33
SDSS10	10.73	9.72	0.05	4.48	...	3	3	9.4
SDSS11	10.85	10.06	0.056	4.88	...	3	3	9.4
SDSS12	10.39	9.51	0.092	4.69	...	3	3	9.62
SDSS13	10.58	9.69	0.064	4.6	...	3	3	9.52
SDSS14	10.92	10.49	0.015	5.01	0.071	3	3	9.94
SDSS15	10.56	10.13	0.051	4.83	...	3	3	9.75
SDSS16	11.18	10.3	0.032	4.67	0.232	3	3	9.18
SDSS17	11.03	10.06	0.04	4.62	...	3	3	9.55
SDSS18	10.69	10.0	0.027	5.07	...	3	3	9.98
SDSS19	11.06	10.47	0.048	4.8	0.083	3	3	9.72
SDSS20	10.77	10.51	0.033	5.11	0.114	3	3	10.02

NOTE—The columns are: (1) Object name (2) Stellar mass (3)(4) Luminosity and its uncertainty at $160\mu\text{m}$ from fluxes as described in §4.1. (5)(6) CO(1–0) luminosity and its uncertainty in solar unit (7) The reference for the stellar mass (8) The reference for the FIR luminosity. (9)(10) [C II] $158\mu\text{m}$ luminosity and its uncertainty used in plots. These values are converted from flux measurements listed in Table 3, using the measurements for extended emission when available (11)(12) Star formation rate and its uncertainty based on the total infrared luminosity derived from the luminosity at $160\mu\text{m}$ as described in §4.1.2 (13) The H_2 mass derived in §4.1.1 using $\alpha_{\text{CO}} = 4.3 (\text{K km s}^{-1} \text{pc}^2)^{-1}$ (Ramos Almeida et al. 2022).

^a Unavailable uncertainty means the corresponding quantity is an upper limit.

References—(1)Koss et al. (2011) (2)Meléndez et al. (2014) (3)Shangguan & Ho (2019)

REFERENCES

- Alatalo, K., Appleton, P. N., Lisenfeld, U., et al. 2014, *ApJ*, 795, 159, doi: [10.1088/0004-637X/795/2/159](https://doi.org/10.1088/0004-637X/795/2/159)
- Alexander, D. M., & Hickox, R. C. 2012, *NewAR*, 56, 93, doi: [10.1016/j.newar.2011.11.003](https://doi.org/10.1016/j.newar.2011.11.003)
- Alonso-Herrero, A., Pereira-Santaella, M., Rieke, G. H., & Rigopoulou, D. 2012, *ApJ*, 744, 2, doi: [10.1088/0004-637X/744/1/2](https://doi.org/10.1088/0004-637X/744/1/2)
- Alonso-Herrero, A., Poulton, R., Roche, P. F., et al. 2016, *MNRAS*, 463, 2405, doi: [10.1093/mnras/stw2031](https://doi.org/10.1093/mnras/stw2031)
- Antonucci, R. 1993, *ARA&A*, 31, 473, doi: [10.1146/annurev.aa.31.090193.002353](https://doi.org/10.1146/annurev.aa.31.090193.002353)
- Appleton, P. N., Guillard, P., Boulanger, F., et al. 2013, *ApJ*, 777, 66, doi: [10.1088/0004-637X/777/1/66](https://doi.org/10.1088/0004-637X/777/1/66)
- Appleton, P. N., Diaz-Santos, T., Fadda, D., et al. 2018, *ApJ*, 869, 61, doi: [10.3847/1538-4357/aaed2a](https://doi.org/10.3847/1538-4357/aaed2a)
- Armus, L., Mazzarella, J. M., Evans, A. S., et al. 2009, *PASP*, 121, 559, doi: [10.1086/600092](https://doi.org/10.1086/600092)
- Astropy Collaboration, Price-Whelan, A. M., Sipőcz, B. M., et al. 2018, *AJ*, 156, 123, doi: [10.3847/1538-3881/aabc4f](https://doi.org/10.3847/1538-3881/aabc4f)
- Bertram, T., Eckart, A., Fischer, S., et al. 2007, *A&A*, 470, 571, doi: [10.1051/0004-6361:20077578](https://doi.org/10.1051/0004-6361:20077578)
- Bolatto, A. D., Wolfire, M., & Leroy, A. K. 2013, *ARA&A*, 51, 207, doi: [10.1146/annurev-astro-082812-140944](https://doi.org/10.1146/annurev-astro-082812-140944)
- Boroson, T. A., & Green, R. F. 1992, *ApJS*, 80, 109, doi: [10.1086/191661](https://doi.org/10.1086/191661)
- Carilli, C. L., & Walter, F. 2013, *ARA&A*, 51, 105, doi: [10.1146/annurev-astro-082812-140953](https://doi.org/10.1146/annurev-astro-082812-140953)
- Casoli, F., & Loinard, L. 2001, in *Astronomical Society of the Pacific Conference Series*, Vol. 235, *Science with the Atacama Large Millimeter Array*, ed. A. Wootten, 305
- Chabrier, G. 2003, *PASP*, 115, 763, doi: [10.1086/376392](https://doi.org/10.1086/376392)
- Chu, J. K., Sanders, D. B., Larson, K. L., et al. 2017, *ApJS*, 229, 25, doi: [10.3847/1538-4365/aa5d15](https://doi.org/10.3847/1538-4365/aa5d15)
- Colditz, S., Beckmann, S., Bryant, A., et al. 2018, *Journal of Astronomical Instrumentation*, 7, 1840004, doi: [10.1142/S2251171718400044](https://doi.org/10.1142/S2251171718400044)
- Davidson-Pilon, C. 2019, *Journal of Open Source Software*, 4, 1317, doi: [10.21105/joss.01317](https://doi.org/10.21105/joss.01317)
- De Looze, I., Cormier, D., Leboutteiller, V., et al. 2014, *A&A*, 568, A62, doi: [10.1051/0004-6361/201322489](https://doi.org/10.1051/0004-6361/201322489)
- Decarli, R., Walter, F., Carilli, C., et al. 2014, *ApJL*, 782, L17, doi: [10.1088/2041-8205/782/2/L17](https://doi.org/10.1088/2041-8205/782/2/L17)
- Díaz-Santos, T., Armus, L., Charmandaris, V., et al. 2013, *ApJ*, 774, 68, doi: [10.1088/0004-637X/774/1/68](https://doi.org/10.1088/0004-637X/774/1/68)
- . 2017, *ApJ*, 846, 32, doi: [10.3847/1538-4357/aa81d7](https://doi.org/10.3847/1538-4357/aa81d7)
- Ellison, S. L., Viswanathan, A., Patton, D. R., et al. 2019, *MNRAS*, 487, 2491, doi: [10.1093/mnras/stz1431](https://doi.org/10.1093/mnras/stz1431)
- Evans, A. S., Frayer, D. T., Surace, J. A., & Sanders, D. B. 2001, *AJ*, 121, 1893, doi: [10.1086/319972](https://doi.org/10.1086/319972)
- Evans, A. S., Solomon, P. M., Tacconi, L. J., Vavilkin, T., & Downes, D. 2006, *AJ*, 132, 2398, doi: [10.1086/508416](https://doi.org/10.1086/508416)
- Evans, A. S., Hines, D. C., Barthel, P., et al. 2009, *AJ*, 138, 262, doi: [10.1088/0004-6256/138/1/262](https://doi.org/10.1088/0004-6256/138/1/262)
- Fadda, D., & Chambers, E. T. 2018, in *American Astronomical Society Meeting Abstracts*, Vol. 231, *American Astronomical Society Meeting Abstracts #231*, 150.11
- Fadda, D., Laine, S., & Appleton, P. N. 2021, *The Astrophysical Journal*, 909, 204, doi: [10.3847/1538-4357/abe0b8](https://doi.org/10.3847/1538-4357/abe0b8)
- Fadda, D., Laine, S., & Appleton, P. N. 2021, *ApJ*, 909, 204, doi: [10.3847/1538-4357/abe0b8](https://doi.org/10.3847/1538-4357/abe0b8)
- Fadda, D., Sutter, J. S., Minchin, R., & Polles, F. 2023a, *ApJ*, 957, 83, doi: [10.3847/1538-4357/acfca1](https://doi.org/10.3847/1538-4357/acfca1)
- Fadda, D., Colditz, S., Fischer, C., et al. 2023b, *AJ*, 166, 237, doi: [10.3847/1538-3881/acffb4](https://doi.org/10.3847/1538-3881/acffb4)
- Feigelson, E. D., & Babu, G. J. 2012, *Modern Statistical Methods for Astronomy: With R Applications* (Cambridge University Press)
- Feigelson, E. D., & Nelson, P. I. 1985, *ApJ*, 293, 192, doi: [10.1086/163225](https://doi.org/10.1086/163225)
- Fischer, C., Beckmann, S., Bryant, A., et al. 2018, *Journal of Astronomical Instrumentation*, 7, 1840003, doi: [10.1142/S2251171718400032](https://doi.org/10.1142/S2251171718400032)
- French, K. D., Yang, Y., Zabludoff, A., et al. 2015, *ApJ*, 801, 1, doi: [10.1088/0004-637X/801/1/1](https://doi.org/10.1088/0004-637X/801/1/1)
- Garcia, K., Narayanan, D., Popping, G., et al. 2023, *slick: Modeling a Universe of Molecular Line Luminosities in Hydrodynamical Simulations*. <https://arxiv.org/abs/2311.01508>
- Glikman, E., Simmons, B., Mailly, M., et al. 2015, *ApJ*, 806, 218, doi: [10.1088/0004-637X/806/2/218](https://doi.org/10.1088/0004-637X/806/2/218)
- Glikman, E., Urrutia, T., Lacy, M., et al. 2012, *ApJ*, 757, 51, doi: [10.1088/0004-637X/757/1/51](https://doi.org/10.1088/0004-637X/757/1/51)
- Greene, J. E., Zakamska, N. L., Ho, L. C., & Barth, A. J. 2011, *ApJ*, 732, 9, doi: [10.1088/0004-637X/732/1/9](https://doi.org/10.1088/0004-637X/732/1/9)
- Grenier, I. A., Casandjian, J.-M., & Terrier, R. 2005, *Science*, 307, 1292, doi: [10.1126/science.1106924](https://doi.org/10.1126/science.1106924)
- Hall, K. P., Stanimirović, S., Lee, M.-Y., Wolfire, M., & Goldsmith, P. 2020, *ApJ*, 899, 23, doi: [10.3847/1538-4357/ab9b86](https://doi.org/10.3847/1538-4357/ab9b86)
- Herrera-Camus, R., Bolatto, A. D., Wolfire, M. G., et al. 2015, *ApJ*, 800, 1, doi: [10.1088/0004-637X/800/1/1](https://doi.org/10.1088/0004-637X/800/1/1)
- Herrero-Illana, R., Privon, G. C., Evans, A. S., et al. 2019, *A&A*, 628, A71, doi: [10.1051/0004-6361/201834088](https://doi.org/10.1051/0004-6361/201834088)
- Hopkins, P. F., Cox, T. J., Kereš, D., & Hernquist, L. 2008a, *ApJS*, 175, 390, doi: [10.1086/524363](https://doi.org/10.1086/524363)
- Hopkins, P. F., Hernquist, L., Cox, T. J., et al. 2006, *ApJS*, 163, 1, doi: [10.1086/499298](https://doi.org/10.1086/499298)
- Hopkins, P. F., Hernquist, L., Cox, T. J., & Kereš, D. 2008b, *ApJS*, 175, 356, doi: [10.1086/524362](https://doi.org/10.1086/524362)

- Howell, J. H., Armus, L., Mazzarella, J. M., et al. 2010, *ApJ*, 715, 572, doi: [10.1088/0004-637X/715/1/572](https://doi.org/10.1088/0004-637X/715/1/572)
- Iserlohe, C., Fischer, C., Vacca, W. D., et al. 2021, *PASP*, 133, 055002, doi: [10.1088/1538-3873/abef76](https://doi.org/10.1088/1538-3873/abef76)
- Kakkad, D., Mainieri, V., Brusa, M., et al. 2017, *MNRAS*, 468, 4205, doi: [10.1093/mnras/stx726](https://doi.org/10.1093/mnras/stx726)
- Kakkad, D., Mainieri, V., Vietri, G., et al. 2023, *MNRAS*, 520, 5783, doi: [10.1093/mnras/stad439](https://doi.org/10.1093/mnras/stad439)
- Kaplan, E. L., & Meier, P. 1958, *Journal of the American Statistical Association*, 53, 457. <http://www.jstor.org/stable/2281868>
- Kennicutt, Robert C., J. 1998, *ARA&A*, 36, 189, doi: [10.1146/annurev.astro.36.1.189](https://doi.org/10.1146/annurev.astro.36.1.189)
- Kim, M., Ho, L. C., & Im, M. 2006, *ApJ*, 642, 702, doi: [10.1086/501422](https://doi.org/10.1086/501422)
- Koss, M., Mushotzky, R., Veilleux, S., et al. 2011, *ApJ*, 739, 57, doi: [10.1088/0004-637X/739/2/57](https://doi.org/10.1088/0004-637X/739/2/57)
- Krips, M., Neri, R., & Cox, P. 2012, *ApJ*, 753, 135, doi: [10.1088/0004-637X/753/2/135](https://doi.org/10.1088/0004-637X/753/2/135)
- Lacy, M., Sajina, A., Petric, A. O., et al. 2007, *ApJL*, 669, L61, doi: [10.1086/523851](https://doi.org/10.1086/523851)
- Lacy, M., Nyland, K., Mao, M., et al. 2018, *ApJ*, 864, 8, doi: [10.3847/1538-4357/aad27d](https://doi.org/10.3847/1538-4357/aad27d)
- Lagache, G., Cousin, M., & Chatzikos, M. 2018, *A&A*, 609, A130, doi: [10.1051/0004-6361/201732019](https://doi.org/10.1051/0004-6361/201732019)
- Larson, K. L., Sanders, D. B., Barnes, J. E., et al. 2016, *ApJ*, 825, 128, doi: [10.3847/0004-637X/825/2/128](https://doi.org/10.3847/0004-637X/825/2/128)
- Li, Q., Narayanan, D., Davè, R., & Krumholz, M. R. 2018, *The Astrophysical Journal*, 869, 73, doi: [10.3847/1538-4357/aaec77](https://doi.org/10.3847/1538-4357/aaec77)
- Liszt, H., & Gerin, M. 2023, *A&A*, 675, A145, doi: [10.1051/0004-6361/202346259](https://doi.org/10.1051/0004-6361/202346259)
- Longinotti, A. L., Kriss, G., Krongold, Y., et al. 2019, *ApJ*, 875, 150, doi: [10.3847/1538-4357/ab125a](https://doi.org/10.3847/1538-4357/ab125a)
- Madden, S. C., Rémy-Ruyer, A., Galametz, M., et al. 2013, *PASP*, 125, 600, doi: [10.1086/671138](https://doi.org/10.1086/671138)
- Madden, S. C., Cormier, D., Hony, S., et al. 2020, *A&A*, 643, A141, doi: [10.1051/0004-6361/202038860](https://doi.org/10.1051/0004-6361/202038860)
- Meléndez, M., Mushotzky, R. F., Shimizu, T. T., Barger, A. J., & Cowie, L. L. 2014, *ApJ*, 794, 152, doi: [10.1088/0004-637X/794/2/152](https://doi.org/10.1088/0004-637X/794/2/152)
- Minchin, R., Fadda, D., Taylor, R., Deshev, B., & Davies, J. 2022, *AJ*, 164, 44, doi: [10.3847/1538-3881/ac746d](https://doi.org/10.3847/1538-3881/ac746d)
- Molina, J., Ho, L. C., Wang, R., et al. 2022, *ApJ*, 935, 72, doi: [10.3847/1538-4357/ac7d4d](https://doi.org/10.3847/1538-4357/ac7d4d)
- Montoya Arroyave, I., Cicone, C., Makroleivaditi, E., et al. 2023, *A&A*, 673, A13, doi: [10.1051/0004-6361/202245046](https://doi.org/10.1051/0004-6361/202245046)
- Narayanan, D., & Krumholz, M. R. 2016, *Monthly Notices of the Royal Astronomical Society*, 467, 50–67, doi: [10.1093/mnras/stw3218](https://doi.org/10.1093/mnras/stw3218)
- Paspaliaris, E. D., Xilouris, E. M., Nersesian, A., et al. 2021, *A&A*, 649, A137, doi: [10.1051/0004-6361/202038605](https://doi.org/10.1051/0004-6361/202038605)
- Petric, A. O., Ho, L. C., Flagey, N. J. M., & Scoville, N. Z. 2015, *ApJS*, 219, 22, doi: [10.1088/0067-0049/219/2/22](https://doi.org/10.1088/0067-0049/219/2/22)
- Petric, A. O., Armus, L., Howell, J., et al. 2011, *ApJ*, 730, 28, doi: [10.1088/0004-637X/730/1/28](https://doi.org/10.1088/0004-637X/730/1/28)
- Petric, A. O., Armus, L., Flagey, N., et al. 2018, *The Astronomical Journal*, 156, 295. <http://stacks.iop.org/1538-3881/156/i=6/a=295>
- Pilbratt, G. L., Riedinger, J. R., Passvogel, T., et al. 2010, *A&A*, 518, L1, doi: [10.1051/0004-6361/201014759](https://doi.org/10.1051/0004-6361/201014759)
- Pineda, J. L., Langer, W. D., Velusamy, T., & Goldsmith, P. F. 2013, *A&A*, 554, A103, doi: [10.1051/0004-6361/201321188](https://doi.org/10.1051/0004-6361/201321188)
- Ramos Almeida, C., Bischetti, M., García-Burillo, S., et al. 2022, *A&A*, 658, A155, doi: [10.1051/0004-6361/202141906](https://doi.org/10.1051/0004-6361/202141906)
- Reyes, R., Zakamska, N. L., Strauss, M. A., et al. 2008, *AJ*, 136, 2373, doi: [10.1088/0004-6256/136/6/2373](https://doi.org/10.1088/0004-6256/136/6/2373)
- Salomé, Q., Krongold, Y., Longinotti, A. L., et al. 2023, *MNRAS*, 524, 3130, doi: [10.1093/mnras/stad2116](https://doi.org/10.1093/mnras/stad2116)
- Salpeter, E. E. 1955, *ApJ*, 121, 161, doi: [10.1086/145971](https://doi.org/10.1086/145971)
- Sanders, D. B., & Mirabel, I. F. 1996, *ARA&A*, 34, 749, doi: [10.1146/annurev.astro.34.1.749](https://doi.org/10.1146/annurev.astro.34.1.749)
- Sanders, D. B., Soifer, B. T., Elias, J. H., et al. 1988a, *ApJ*, 325, 74, doi: [10.1086/165983](https://doi.org/10.1086/165983)
- Sanders, D. B., Soifer, B. T., Elias, J. H., Neugebauer, G., & Matthews, K. 1988b, *ApJL*, 328, L35, doi: [10.1086/185155](https://doi.org/10.1086/185155)
- Sargsyan, L., Leboutellier, V., Weedman, D., et al. 2012, *ApJ*, 755, 171, doi: [10.1088/0004-637X/755/2/171](https://doi.org/10.1088/0004-637X/755/2/171)
- Schmidt, M., & Green, R. F. 1983, *ApJ*, 269, 352, doi: [10.1086/161048](https://doi.org/10.1086/161048)
- Scoville, N. Z., Frayer, D. T., Schinnerer, E., & Christopher, M. 2003, *ApJL*, 585, L105, doi: [10.1086/374544](https://doi.org/10.1086/374544)
- Shangguan, J., & Ho, L. C. 2019, *ApJ*, 873, 90, doi: [10.3847/1538-4357/ab0555](https://doi.org/10.3847/1538-4357/ab0555)
- Shangguan, J., Ho, L. C., Bauer, F. E., Wang, R., & Treister, E. 2020, *ApJS*, 247, 15, doi: [10.3847/1538-4365/ab5db2](https://doi.org/10.3847/1538-4365/ab5db2)
- Shangguan, J., Ho, L. C., Li, R., et al. 2019, *ApJ*, 870, 104, doi: [10.3847/1538-4357/aaf21a](https://doi.org/10.3847/1538-4357/aaf21a)
- Shangguan, J., Ho, L. C., & Xie, Y. 2018, *ApJ*, 854, 158, doi: [10.3847/1538-4357/aaa9be](https://doi.org/10.3847/1538-4357/aaa9be)
- Smirnova-Pinchukova, I., Husemann, B., Busch, G., et al. 2019, *A&A*, 626, L3, doi: [10.1051/0004-6361/201935577](https://doi.org/10.1051/0004-6361/201935577)
- Solomon, P. M., Downes, D., Radford, S. J. E., & Barrett, J. W. 1997, *ApJ*, 478, 144, doi: [10.1086/303765](https://doi.org/10.1086/303765)
- Stierwalt, S., Armus, L., Surace, J. A., et al. 2013, *ApJS*, 206, 1, doi: [10.1088/0067-0049/206/1/1](https://doi.org/10.1088/0067-0049/206/1/1)
- Symeonidis, M., Willner, S. P., Rigopoulou, D., et al. 2008, *MNRAS*, 385, 1015, doi: [10.1111/j.1365-2966.2008.12899.x](https://doi.org/10.1111/j.1365-2966.2008.12899.x)
- Tombesi, F., Cappi, M., Reeves, J. N., et al. 2010, *A&A*, 521, A57, doi: [10.1051/0004-6361/200913440](https://doi.org/10.1051/0004-6361/200913440)
- U, V., Sanders, D. B., Mazzarella, J. M., et al. 2012, *ApJS*, 203, 9, doi: [10.1088/0067-0049/203/1/9](https://doi.org/10.1088/0067-0049/203/1/9)

- Urrutia, T., Lacy, M., & Becker, R. H. 2008, *ApJ*, 674, 80, doi: [10.1086/523959](https://doi.org/10.1086/523959)
- Vacca, W., Clarke, M., Perera, D., Fadda, D., & Holt, J. 2020, in *Astronomical Society of the Pacific Conference Series*, Vol. 527, *Astronomical Data Analysis Software and Systems XXIX*, ed. R. Pizzo, E. R. Deul, J. D. Mol, J. de Plaa, & H. Verkouter, 547
- Veilleux, S., Rupke, D. S. N., Kim, D. C., et al. 2009, *ApJS*, 182, 628, doi: [10.1088/0067-0049/182/2/628](https://doi.org/10.1088/0067-0049/182/2/628)
- Villar-Martín, M., Rodríguez, M., Drouart, G., et al. 2013, *MNRAS*, 434, 978, doi: [10.1093/mnras/stt1014](https://doi.org/10.1093/mnras/stt1014)
- Villforth, C., Hamilton, T., Pawlik, M. M., et al. 2017, *MNRAS*, 466, 812, doi: [10.1093/mnras/stw3037](https://doi.org/10.1093/mnras/stw3037)
- Wolfire, M. G., McKee, C. F., Hollenbach, D., & Tielens, A. G. G. M. 2003, *ApJ*, 587, 278, doi: [10.1086/368016](https://doi.org/10.1086/368016)
- Wylezalek, D., Cicone, C., Belfiore, F., et al. 2022, *MNRAS*, 510, 3119, doi: [10.1093/mnras/stab3356](https://doi.org/10.1093/mnras/stab3356)
- Xie, Y., Ho, L. C., Zhuang, M.-Y., & Shangguan, J. 2021, *ApJ*, 910, 124, doi: [10.3847/1538-4357/abe404](https://doi.org/10.3847/1538-4357/abe404)
- Yamashita, T., Komugi, S., Matsuhara, H., et al. 2017, *ApJ*, 844, 96, doi: [10.3847/1538-4357/aa7af1](https://doi.org/10.3847/1538-4357/aa7af1)
- Young, E. T., Becklin, E. E., Marcum, P. M., et al. 2012, *ApJL*, 749, L17, doi: [10.1088/2041-8205/749/2/L17](https://doi.org/10.1088/2041-8205/749/2/L17)
- Zakamska, N. L., Gómez, L., Strauss, M. A., & Krolik, J. H. 2008, *AJ*, 136, 1607, doi: [10.1088/0004-6256/136/4/1607](https://doi.org/10.1088/0004-6256/136/4/1607)
- Zakamska, N. L., Schmidt, G. D., Smith, P. S., et al. 2005, *AJ*, 129, 1212, doi: [10.1086/427543](https://doi.org/10.1086/427543)
- Zakamska, N. L., Lampayan, K., Petric, A., et al. 2016, *MNRAS*, 455, 4191, doi: [10.1093/mnras/stv2571](https://doi.org/10.1093/mnras/stv2571)
- Zanella, A., Daddi, E., Magdis, G., et al. 2018, *MNRAS*, 481, 1976, doi: [10.1093/mnras/sty2394](https://doi.org/10.1093/mnras/sty2394)

